Modeling and Extending RSS-based Intrusion Detection Bound via WiFi Signals

Linqing Gui, Yuting Yang, Yiping Zuo, Fu Xiao, and Schahram Dustdar, *Fellow, IEEE*

***Abstract*—Leveraging ubiquitous WiFi infrastructures, intrusion detection methods based on Received Signal Strength (RSS) offer compelling advantages, including cost-effectiveness and privacy protection. However, existing RSS-based intrusion detection solutions fall short of accurately estimating and extending the WiFi sensing bound. In this paper, we propose a novel model of motion-disturbed RSS and design an effective R-ratio indicator to extend the intrusion detection bound. Specifically, we first establish a general model of motion-disturbed RSS and derive the blocked area and reflection area in this RSS model. Then, we define the WiFi intrusion detection bound and propose a performance indicator called R-ratio to extend the bound with RSS. Furthermore, based on the statistical properties of noise, we design an efficient filter to further weaken the noise. We also propose two new methods to further extend intrusion detection bound. Extensive experimental results demonstrate that the proposed power sum ratio based intrusion detection method can approximately double the WiFi intrusion detection bound compared to other methods with raw RSS data, and our developed motion-disturbed RSS model can provide valuable insights and guidance to the intrusion detection system.**

***Index Terms*—WiFi, intrusion detection, RSS, sensing bound.**

I. Introduction

In recent years, with the rapid development of wireless technologies, intrusion detection gains increasing attention and has great potential in many applications, such as border protection [1], smart home [2], elderly healthcare [3]. Various techniques have been proposed for intrusion detection, such as video-based [4], infrared-based [5], sound-based [6] and wearable-based [7] approaches. By producing real-time live images, video-based approaches can create severe privacy problems for home users. Passive infrared approaches achieve better privacy protection but have limited detection angle/range. Although sound-based approach support non-LoS (NLoS) scenarios, the detection accuracy is easily affected by environment noise. Wearable-based approaches attach the sensors to the body, which can be inconvenient in certain scenarios. Therefore, there is a strong desire for passive intrusion detection methods that are ubiquitous, low-cost, and privacy-friendly.

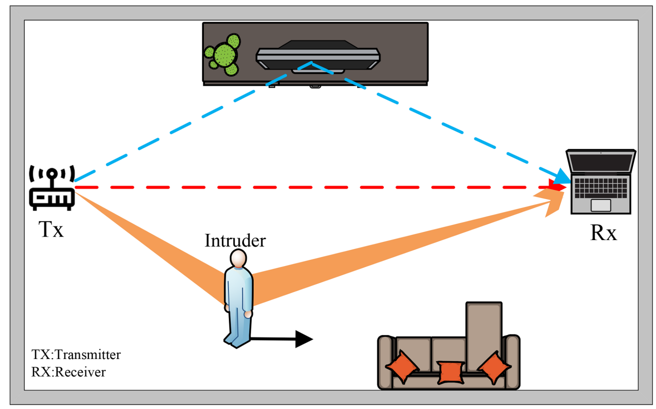

Fig. 1. The setup for intrusion detection with WiFi devices.

WiFi-based intrusion detection methods [8], [9] can meet the aforementioned requirements. As shown in Fig. 1, indoor widely deployed WiFi devices can be used to detect intrusion in a passive way, as the intruder is not required to carry any electronic devices. Up to now, a number of received WiFi signal measurements, such as Received Signal Strength (RSS) [8] and Channel State Information (CSI) [9], have been employed for passive detection of moving targets by identifying any changes. The basic principle of WiFi-based methods lies in the fact that the key features of sensitive wireless signals change with nearby intrusions. Currently, WiFi-based methods can effectively detect human motion by exploiting variations in RSS measurements [10], [11]. When connecting more smart devices, such as refrigerator, TV, and air conditioner, the RSS-based intrusion detection system can extend the monitoring area.

In WiFi-based intrusion detection systems, compared to CSI, RSS has two main advantages. 1) Ease of acquisition: Since WiFi devices such as smartphones and routers all support RSS measurement, RSS is very easy to obtain. In contrast, obtaining

Received 6 November 2024; revised 12 September 2025; accepted 14 October 2025. Date of publication 28 October 2025; date of current version 4 February 2026. This work was supported in part by the National Key R&D Program of China under Grant 2023YFB3107500, in part by the National Science Fund for Distinguished Young Scholars under Grant 62125203, and in part by the National Natural Science Foundation of China under Grant 62372246 and Grant 62301279. Recommended for acceptance by N. Shlezinger. *(Corresponding author: Fu Xiao.)*

Linqing Gui is with the School of Computer, Nanjing University of Posts and Telecommunications, Nanjing 210023, China, also with the State Key Laboratory of Tibetan Intelligence, Nanjing 210023, China, also with the Jiangsu Provincial Key Laboratory of Internet of Things Intelligent Perception and Computing, Nanjing 210023, China, and also with the State Key Laboratory of Tibetan Intelligence, Qinghai Normal University, Xining 810016, China (e-mail: guilq@njupt.edu.cn).

Yuting Yang, Yiping Zuo, and Fu Xiao are with the School of Computer, Nanjing University of Posts and Telecommunications, Nanjing 210023, China, also with the State Key Laboratory of Tibetan Intelligence, Nanjing 210023, China, and also with the Jiangsu Provincial Key Laboratory of Internet of Things Intelligent Perception and Computing, Nanjing 210023, China (e-mail: 1222045632@njupt.edu.cn; zuoyiping@njupt.edu.cn; xiaof@njupt.edu.cn).

Schahram Dustdar is with the Research Division of Distributed Systems, TU Wien, 1040 Vienna, Austria, and also with the ICREA Research Professor, UPF, 08010 Barcelona, Spain (e-mail: dustdar@dsg.tuwien.ac.at).

Digital Object Identifier 10.1109/TMC.2025.3626539

CSI requires more complex hardware support, such as firmware-modified WiFi network interface cards [12], which adds to the cost and complexity of the system. 2) Simplicity and real-time capability: Since RSS only contains simple signal strength information, it can easily support real-time intrusion detection for common WiFi devices with limited computing resources. On the contrary, CSI contains amplitude and phase information at dozens of subcarriers, having much richer information than RSS, but this richness information also increases computational complexity and requires more powerful computing resources [13], [14]. Although RSS may have lower accuracy and sensitivity in certain aspects, in many application scenarios, especially where real-time requirements are high, and hardware resources are limited, choosing RSS is a more practical and feasible option.

In our daily lives, contactless sensing of wireless signals is widely acknowledged as a highly promising method. In practical applications, numerous RSS-based sensing applications necessitate prior knowledge of human presence in the designated sensing area. However, a definitive solution to accurately determine the entry of a person into a specific area remains elusive, leading to imprecise bound sensing. This limitation constrains the practical application of RSS-based sensing in real-life scenarios. By analyzing existing RSS-based intrusion detection works, we find that existing works have some limitations in calculating the intrusion detection bound and extending the sensing range. First, in the current study, there is a lack of precise intrusion detection bound models, which hinders our accurate estimation of the bound. When estimating precise intrusion detection bounds, the following challenges are encountered: 1) Environmental complexity: In a complex and changeable environment, a wide variety of obstacles, multi-layered buildings, etc. will affect the precise bounds. 2) Sensor error: Since RSS signals have problems such as multipath transmission and signal attenuation, these problems will affect the intrusion detection bound. 3) Dynamic environment: When there are moving obstacles or people in the environment, the intrusion detection bound will also change accordingly. It is difficult for current intrusion detection methods to effectively detect human motion at long distances. The reason is that when the intruder is distant from the transmitter and receiver, RSS variation caused by intrusion is very weak, easily affected by the noises including the impulse noise and the measurement noise. Second when extending our sensing range, we face the challenges from multipath interference. In order to increase sensing range, multipath interference should be mitigated. When detecting a more distant intruder, RSS variation caused by the intrusion is weaker, but multipath interference caused by walls and furniture becomes relatively stronger. It is more difficult to separate RSS variation caused by the intrusion from the RSS that mixed with multipath interference.

To tackle the aforementioned challenges, in this paper, we explored a novel model of motion-disturbed RSS to precisely characterize the intrusion detection, then proposed an effective R-ratio indicator, an efficient filter and two new methods to extend intrusion detection bound. The main contributions of this work are summarized as follows.

- We propose a novel model of motion-disturbed RSS for the first time to precisely characterize the intrusion detection bound. By analyzing the influence of the intruder's body size and angle on RSS and deriving the blocked area and reflection area, we successfully establish a theoretical relationship between human motion and RSS changes. Our developed motion-disturbed RSS model can provide valuable insights and guidance to extend intrusion detection bound.
- According to the proposed RSS model, we propose R-ratio indicator and an efficient filter to enhance the motion signal, then propose two new methods to extend intrusion detection bound. By combining RSS data at different moments, R-ratio can mitigate the impact of impulse noise on amplitude. Furthermore, based on the statistical properties of noise, the designed filter can further weaken the measurement noise. We additionally present two customized intrusion detection methods to further extend intrusion detection bound.
- Extensive experimental results demonstrate that the proposed R-ratio-based intrusion detection method can approximately double the WiFi intrusion detection bound compared to other methods with raw RSS data, effectively extending the sensing range from 4 to 8 meters. In line with the proposed motion-disturbed RSS model, the experimental results also show that body size and intrusion angle have a signiffcant impact on the sensing bound.

The rest of this paper is organized as follow. Section II introduces the most related work. Section III presents the derivation of motion-disturbed RSS model. Analysis of broadening the bound of intrusion detection is illustrated in Section IV. Then the experiment results together with the analysis is presented in Section V. Conclusions are provided in Section VI.

II. Related Work

In recent years, the utilization of WiFi signals for contactlessly detecting human presence including intrusion detection has gained prominence. Here, intrusion detection can be regarded as a special case of human presence detection, since the target to be detected is an intruder. So in this section we first introduce existing work on device-free human presence detection using WiFi signals, although only a few of them use WiFi RSS. As RSS model is a fundamental issue for device-free applications including intrusion detection, we then introduce typical existing RSS models. Finally, current research on sensing bound are introduced since we aim to extend intrusion detection bound.

A. Device-Free Human Presence Detection Using WiFi Signals

Most existing device-free human presence detection systems used WiFi CSI because CSI has rich amplitude and phase information at multiple subcarriers. In [15], intrusion was determined by monitoring both the amplitude of WiFi CSI and changes in the angle of arrival distribution. Suspicious activities in highly sensitive areas were surveilled in [16] by analyzing both amplitude and phase of WiFi CSI to ascertain the presence of intruders. In [17], an intrusion detection bound model based on WiFi CSI was derived, then a practical system was designed accordingly to estimate real intrusion detection bound. The blind spots of video surveillance systems were fixed in [18] by sensing the intrusion with existing WiFi infrastructure. To that end, a CSI-based intrusion detection system was designed to guide the deployment of WiFi devices. Although CSI has much richer information than RSS, the computational complexity of CSI-based methods is much higher. Moreover, obtaining CSI requires more complex hardware support. In contrast, RSS has prominent advantages on ubiquity, simplicity and real-time capability. In [19], based on three different change primitives in RSS, the target closed to the receiver was recognized through pattern matching. RSS characteristic profiles were built in [8] by using non-parametric statistical method, and a joint detection scheme by using multiple WiFi node pairs was used to detect nearby intrusions. By analyzing existing work, we find that the sensing bound in existing RSS-based systems is still limited. It should be derived and extended, so that the intrusion can be detected as early as possible.

B. RSS Model in Device-Free Applications

In [20], the target was regarded as a cylinder and a cylinder model was proposed to characterize the RSS variation. Then a saddle surface model was proposed in [21] to represent the shadowing effect of the target on wireless links. Rectangular shape was used to simulate environmental obstacles such as buildings [22]. Cube models were also frequently used to represent human body, which can be found in [23], [24], [25]. More complex diffraction models were then proposed to characterize RSS. For example, four diffraction models were investigated in [26], where the human body was positioned between the transmitter and receiver. A simplified human body model based on the scalar diffraction theory was proposed in [27], where the distance between the person and the wireless link was less than 1 m. An analytically tractable model based on diffraction theory was then proposed in [28] to detect the presence of a moving object which was near the transmitting/receiving devices. Based on a diffraction-based sensing model, more than 70% of RF signal energy was transferred via the First Fresnel Zone between a pair of Wi-Fi transceivers [29], but the target should be close to the line-of-sight path between the transmitter and receiver. Based on the above analysis, diffraction has a significant impact only when the target is near the line-of-sight path between the transmitter and receiver. However, in intrusion detection systems, the intruder is normally far away from the transmitter and receiver, thus significantly weakening the effect of diffraction.

C. WiFi-Based Device-Free Sensing Bound

The research on device-free sensing bound have emerged these years. Zhang et al. [30] formulated a mathematical model establishing a relationship between an individual's location and the detectability of respiration within the First Fresnel Zone (FFZ). Zeng et al. [31] introduced a CSI-ratio model to tackle the issue of blind spots in respiration detection, consequently extending the sensing range. This approach required the synchronization of CSI stream clocks between two receiving antennas. Li et al. [32] derived a novel metric, DCM-CSI, from the conjugate multiplication of CSI between two antennas. Using this metric, a stable threshold line was identified to distinguish direct and indirect signals. Subsequently, the environmental walls were leveraged to establish sensing bounds. However, existing works are all based on CSI-based sensing bound, and there are few research work on RSS-based sensing bound detection methods. Therefore, our work is to precisely characterize and model the intrusion detection bound by analyzing RSS disturbed by human motion.

III. Modeling RSS-Based Intrusion Detection Bound

In this section, we first provide the definition of intrusion detection bound. Then we build a general model of motion-disturbed RSS. To refine this RSS model and gain a more comprehensive understanding, we derive the detail expressions for both the blocked area and the reflection area within the basic model. Finally, we derive an intrusion detection bound model based on the RSS model.

A. Definition of Intrusion Detection Bound

In WiFi-based sensing systems, the sensing range is primarily influenced by signal attenuation and propagation characteristics. The concept of the intrusion detection bound holds significant importance as it establishes the maximum distance at which the system can reliably detect human movement. The farthest position where the intruder can be detected corresponds to the maximum intrusion detection range, i.e., the intrusion detection bound.

Specifically, when the RSS features extracted by the human motion detection method are greater than the threshold, the maximum intrusion detection range is recorded as the intrusion detection bound. Then the Intrusion Detection Bound (IDB) can be expressed as:

$$IDB = \max\left(d_{TP} | RSS_{ft} > RSS_{th}\right), \tag{1}$$

where d_{TP} is the distance between intruder and transceiver, RSS_{ft} is the extracted RSS feature, RSS_{th} is the threshold.

B. A General Model of Motion-Disturbed RSS

We build a general model of motion-disturbed RSS by analyzing multipath propagation. In an indoor environment, the signal arriving at the receiver is a superposition of signals coming from multiple paths. Therefore, the RSS depends on the amplitude and phase of multipath signals at the receiver. The channel frequency response (CFR) at the *i*-th subcarrier and time *t* can be expressed as follows:

$$H\left(f_i, t\right) = \sum_{l=1}^{L} a_l\left(f_i, t\right) e^{\frac{-j2\pi d_l(t)}{\lambda}} + \varepsilon(t), \tag{2}$$

where L is the number of all paths, f_i is the subcarrier frequency, j is imaginary unit, λ is the wavelength of the signal, $a_l(f_i, t)$ represents the amplitude attenuation and phase change of the l-th path, $d_l(t)$ is the distance of the l-th path, and $\varepsilon(t)$ is the measurement noise of $H(f_i, t)$. According to the basic relation

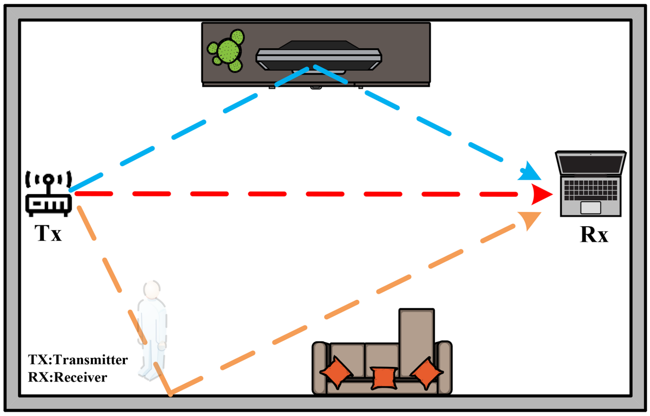

Fig. 2. Multiple path propagation of WiFi signal.

between RSS and CFR [33], [34], if the transmitted power is denoted by P_t, then the RSS can be expressed as:

$$RSS(t) = \sum_{i=1}^{N_f} |H(f_i, t)|^2 \times P_t, \tag{3}$$

where N_f is the number of subcarriers. Due to strong correlation between adjacent subcarriers [35], [36], the expression of RSS in (3) can be approximated as :

$$RSS(t) = N_f \, |H(f, t)|^2 \, P_t, \tag{4}$$

where $H(f, t)$ is the frequency of center subcarrier.

When the intruder comes, $H(f, t)$ is typically the superposition of static component and dynamic component, and is affected by noise. According to the reference [37], $H(f, t)$ can be written as:

$$H(f, t) = A_{noise} e^{-j\theta_{offset}(f,t)} \left(H_s(f) + H_d(f, t) + \varepsilon(f, t)\right), \tag{5}$$

where A_{noise} is the impulse noise in amplitude and $e^{-j\theta_{offset}(f,t)}$ is the random phase offset, $H_s(f)$ is static component, and $H_d(f, t)$ is dynamic component. $H_s(f)$ includes the LoS path and the reflection paths via static objects such as walls and furntiure, while $H_d(f, t)$ corresponds to dynamic reflection paths via moving objects such as an intruder and changes with human movements. Here, the reflection is not specular reflection but actually scatter, because specular reflection requires objects have extremely smooth surface [38] which does not apply to objects like humans and walls.

As illustrated in Fig. 2, when there is no person in an indoor environment, the static signal arriving at the receiver is the superposition of signals coming from all static paths. In the multipath-rich environment, the shortest path is directly from the transmitter to the receiver if the LoS propagation is present. Other paths comprise reflective paths on which the transmitted signal is reflected once or more times at various kinds of reflectors such as the walls and floors. Each reflection causes corresponding reflection loss. Therefore, $H_s(f)$ can be expressed as follows:

$$H_s(f) = \sum_{k \in P_s} \prod_{n=1}^{N_k} S_k^{(n)} \Gamma_k^{(n)} a_k(f) e^{\frac{-j2\pi d_k}{\lambda}} + \varepsilon(f), \tag{6}$$

where P_s is the set of all static paths, $a_k(f)$ represents the amplitude attenuation and initial phase of the k-th path, and d_k is the distance of the k-th path. N_k is the number of reflections on the k-th path, and $S_k^{(n)}$ is the reflection area of the n-th reflection on the k-th path. $\Gamma_k^{(n)}$ is the reflection coefficient per unit reflection area of the n-th reflection on the k-th path. According to (6), multiple reflections dramatically weaken the signal arriving at the receiver, so we can only consider once-reflection path. It is also more consistent with the instantaneous RSS, because once-reflection path is the-shortest reflection link, while the RSS is supposed to be measured in very short period of time. Then (6) can be abbreviated as:

$$H_s(f) = \sum_{k \in P_s} S_k \Gamma_k a_k(f) e^{\frac{-j2\pi d_k}{\lambda}} + \varepsilon(f), \tag{7}$$

where S_k is the reflection area of once reflection on the k-th path, Γ_k is the reflection coefficient per unit area of once reflection on the k-th path. Γ_k can be expressed as a function of the signal incident angle and the permittivity of the reflection surface [39].

Since the antennas in our Wi-Fi device exhibit vertical polarization, the reflection coefficient follows the equation below according to references [39], [40]:

$$\Gamma_{\mathrm{k}} = \frac{\cos\phi - \sqrt{\varepsilon_r - \sin^2\phi}}{\cos\phi + \sqrt{\varepsilon_r - \sin^2\phi}}, \tag{8}$$

where ϕ is the signal incident angle, ε_r is the complex relative permittivity of reflector.

As shown in Fig. 1, when someone appears in an indoor environment, the RSS is disturbed because some static paths are blocked by the human body and these paths change their reflectors to the human body. $H_d(f, t)$ corresponds to signals which are reflected and blocked by the human body and can be written as:

$$\begin{aligned} H_d(f, t) &= S_{mo}(t) \Gamma_{mo} a_{mo}(f, t) e^{\frac{-j2\pi d_{mo(t)}}{\lambda}} \\ &\quad - S_{bl}(t) \Gamma_{bl} a_{bl}(f, t) e^{\frac{-j2\pi d_{bl(t)}}{\lambda}} + \varepsilon(f, t) \end{aligned} \tag{9}$$

where $S_{mo}(t)$ is the reflection area on the human body, $S_{bl}(t)$ is the area blocked by the human body, Γ_{mo} is the reflection coefficient per unit reflection area, and Γ_{bl} is the reflection coefficient per unit blocked area. $a_{mo}(f, t)$ and $a_{bl}(f, t)$ represent the amplitude attenuation and initial phase of the human reflection path and the blocked path, respectively. $d_{mo}(t)$ and $d_{bl}(t)$ are the distance of the human reflection path and the blocked path, respectively.

When the distance between the intruder and the transmitter changes, it causes variation in the signal incidence angle, which correspondingly affects the reflection coefficient. But we find that the variation range of the reflection coefficient caused by the change of signal incidence angle is small in our experiment scenario. Therefore, our RSS model selects first-order reflection with the shortest propagation distance.

Since static path signals in the indoor environment remain constant over a short period of time, combining (3), (5), and (9),

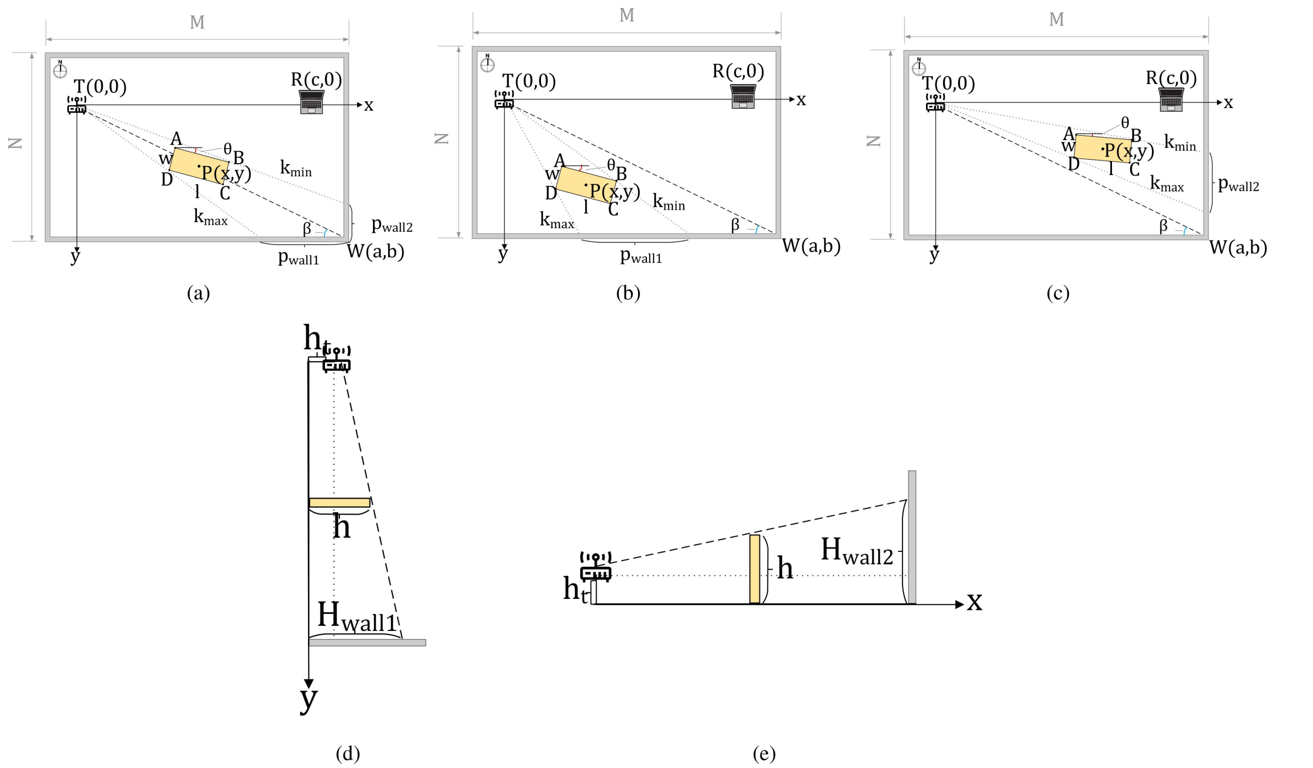

Fig. 3. The projection of the transmitted signal blocked by the human body on the wall: (a) Top view projected on both walls, (b) Top view projected only on south wall, (c) Top view projected only on east wall, (d) Side view projected on the south wall, (e) Side view projected on the east wall.

RSS can be written as:

$$\begin{aligned} RSS(t) = N_f|&A_{noise}e^{-j\theta_{offset}(f,t)}(H_s(f) \\ &+ S_{mo}(t)\Gamma_{mo}a_{mo}(f,t)e^{\frac{-j2\pi d_{mo}(t)}{\lambda}} \\ &- S_{bl}(t)\Gamma_{bl}a_{bl}(f,t)e^{\frac{-j2\pi d_{bl}(t)}{\lambda}} + \varepsilon(f,t))|^2 \times P_t. \end{aligned} \tag{10}$$

We can observe that both the blocked area and reflection area have a significant impact on RSS. In the next subsection, we will derive the blocked area and reflection area in detail.

C. Derivation of the Blocked Area in RSS Model

Based on the equation (10), S_{bl} represents the area blocked by the human body, which changes with the orientation and position of the human body. We approximate the area blocked by the human body by calculating the projected area on the wall. As shown in Fig. 3, the length of the room is M and the width is N. The transmitter is located at distances a and b from the east and south walls, respectively. The distance between the transmitter and the receiver is c, and the connecting line between the transmitter and the receiver is parallel to the south wall. To establish a two-dimensional coordinate system, the transmitter is at the origin. We designate the east direction as the positive x-axis direction and the south direction as the positive y-axis direction. We model the human body as a cube with dimensions of length, width, and height, denoted as l, w, and h, respectively. The angle between the line TW and the south wall is β, the angle between the front of the human body and the south wall is θ, and the clockwise direction of the angle is defined as the positive direction. The person locates at point $P(x,y)$, and the shape of the person when viewed from above is a rectangle of length l and width w, with the four vertices denoted as A, B, C, and D, respectively.

We can easily calculate the coordinates of the four vertices. Subsequently, we calculate the slopes between the transmitter and these vertices to determine the boundaries of the blocked area. The area blocked by the human body can be determined by the maximum slope denoted as $k_{\max}$ and the minimum slope denoted as $k_{\min}$. These two slopes correspond to the left and right boundaries of the blocked area, respectively. As illustrated in Fig. 3(a)–(c), the transmitted signals blocked by the human body are projected only on the south wall or only on the east wall or on both walls. The projected height on the south wall and the east wall are shown in Fig. 3(d) and (e).

According to the triangle proportionality property, the blocked area projected on the wall can be expressed as:

$$S_{bl} = S_{bl1} + S_{bl2}, \tag{11}$$

where

$$\begin{aligned} S_{bl1} &= P_{wall1} \times H_{wall1} \\ &= \max\left(\frac{1}{\max(k_{\min}, \tan\beta)} - \frac{1}{k_{\max}}, 0\right)\left(\frac{b(h-h_t)}{y} + h_t\right)b, \end{aligned} \tag{12}$$

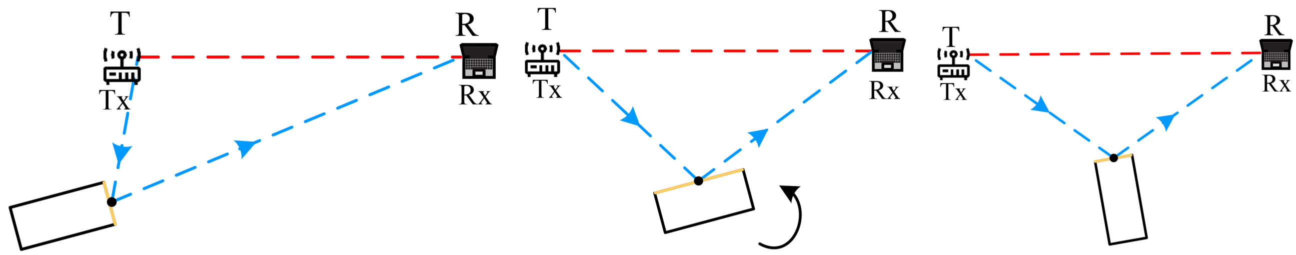

(a) Orientation I, location I (b) Orientation I, location II (c) Orientation II, location II

Fig. 4. Scatter area of the human body at different positions and orientations.

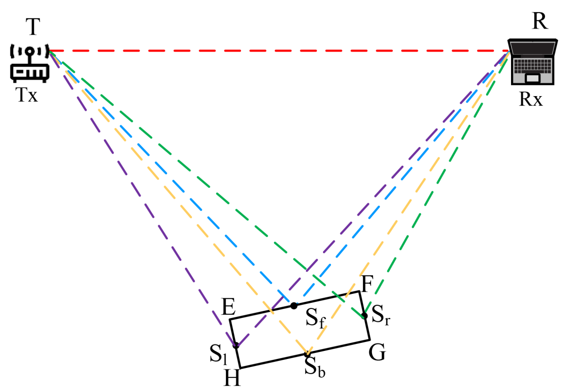

Fig. 5. Top view of the connection between the central points of the four surfaces of the human body and the transmitter and receiver.

$$S_{bl2} = P_{wall2} \times H_{wall2}$$
$$= \max(\min(k_{\max}, \tan\beta) - k_{\min}, 0)\left(\frac{a(h-h_t)}{x} + h_t\right)a, \tag{13}$$

with $k_{\max} = \max(k_1, k_2, k_3, k_4)$, $k_{\min} = \min(k_1, k_2, k_3, k_4)$ and $\tan\beta = \frac{b}{a}$. Here, $k_1 = \frac{y-l2\sin\theta-w2\cos\theta}{x+w2\sin\theta-l2\cos\theta}$, $k_2 = \frac{y+l2\sin\theta-w2\cos\theta}{x+w2\sin\theta+l2\cos\theta}$, $k_3 = \frac{y+l2\sin\theta+w2\cos\theta}{x-w2\sin\theta+l2\cos\theta}$, and $k_4 = \frac{y-l2\sin\theta+w2\cos\theta}{x-w2\sin\theta-l2\cos\theta}$. When $\min(k_{\max}, \tan\beta) \leq k_{\min}$, then $S_{bl} = S_{bl2}$. At this time, the blocked area is only projected on the east wall, as shown in Fig. 3(e). When $\frac{1}{\max(k_{\min},\tan\beta)} \leq \frac{1}{k_{\max}}$, $S_{bl2} = 0$, then $S_{bl} = S_{bl1}$. At this time, the blocked area is only projected on the south wall, as shown in Fig. 3(d).

D. Derivation of the Reflection Area in RSS Model

As observed in Fig. 4(a) and (b), the reflection area varies when a person is in the same orientation but at different locations. Similarly, when a person is at the same location but in different orientations, the reflection area is also different, as shown in Fig. 4(b) and (c). Next, we introduce how to calculate the effective reflection area of the human body.

Fig. 5 displays a top view of the central points of the four surfaces of the human body. The human body is regarded as a rectangle, with four vertices marked as E, F, G, and H, respectively. In addition, S_f, S_b, S_l, and S_r are the central points of the front, back, left and right surfaces of the human body, respectively.

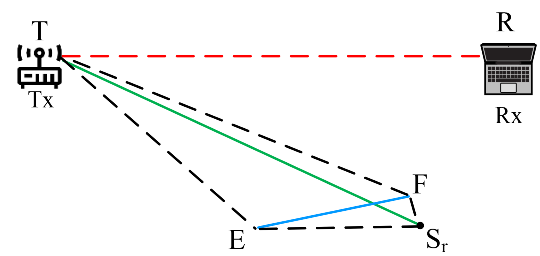

Fig. 6. Top view of the connection between the central point of the right surface of the human body and the transmitter.

For the paths TS_lR, TS_rR, and TS_bR, electromagnetic waves need to penetrate the human body to reach the receiver. However, penetrating the human body is too difficult for WiFi signals, because approximately 70% of the human body is composed of water, while electromagnetic waves experience significant attenuation in water. Therefore, the surfaces of the human body where the points S_b, S_l, and S_r are located cannot be regarded as reflection surfaces. In contrast, as to the path TS_fR, the signal can reach the receiver only through one reflection. Thus, the surface of the human body where the point S_f is located can be regarded as the effective reflection surface and its area is the effective reflection area.

Based on the above analysis, the determination of the effective reflection surface depends on whether the line between the central point of a particular surface of the human body and the transceiver passes through the human body. Take the right surface of the human body (i.e. FG surface) as an example, if line segment TS_r or RS_r intersects with line segment EF, EH or GH, the FG surface is not the effective reflection surface; otherwise, the FG surface is the effective reflection surface. The intersection of two line segments is determined by computing a vector cross-product. Take the line segment TS_r and line segment EF for example, as illustrated in Fig. 6. Points E and F are on opposite sides of line segment TS_r, so vectors $\overrightarrow{TE}$ and $\overrightarrow{TF}$ are on opposite sides of vector $\overrightarrow{TS_r}$ resulting in cross products with different signs. Similarly, points T andS_r are on opposite sides of line segment EF, so vectors $\overrightarrow{ET}$ and $\overrightarrow{ES_r}$ are on opposite sides of vector $\overrightarrow{EF}$, resulting in cross products with different signs. When both conditions are met, the two line segments intersect. We use $I(Line1, Line2)$ to denote wheather the two line segments intersect or not, then we have

$$I\left(TS_r, EF\right) = \begin{cases} 1, \text{if} \begin{cases} \left(\overrightarrow{ET} \times \overrightarrow{EF}\right) \cdot \left(\overrightarrow{ES_r} \times \overrightarrow{EF}\right) \leq 0 \\ \left(\overrightarrow{TE} \times \overrightarrow{TS_r}\right) \cdot \left(\overrightarrow{TF} \times \overrightarrow{TS_r}\right) \leq 0 \end{cases} \\ 0, \text{otherwise} \end{cases} \tag{14}$$

Theoretically, beside S_r, any point on the FG segment can be chosen to determine whether FG surface acts as a reflection surface. The reason is that no matter which point is selected, FG surface can be determined as a reflection surface if the line between the selected point and the transceiver never passes through the human body. Nevertheless, without loss of generality, also for the ease of computation, the central point is chosen. Furthermore, we use $J(Surface)$ to denote whether a particular surface of the human body is the reflection surface or not. Taking FG surface as an example, we have

$$J(FG) = \sum\nolimits_{Line_{TR} \in \{TS_r,\ RS_r\}} \sum\nolimits_{Line_S \in \{EF,\ EH,\ GH\}} I(Line_{TR},\ Line_S), \tag{15}$$

If $J(FG)$ is 0, the FG surface is regarded as the reflection surface. Otherwise, the FG surface is not the reflection surface. The same is true for other surfaces. In summary, the effective reflection area of the human body can be expressed as:

$$S_{mo} = \begin{cases} l \times h, \text{if } J(EF) = 0 \parallel J(GH) = 0 \\ w \times h, \text{if } J(EH) = 0 \parallel J(FG) = 0 \\ 0, \text{otherwise} \end{cases}. \tag{16}$$

At this point, we have successfully derived the blocked area S_{bl} and the reflection area S_{mo}. Substituting them into equation (10), we can get the complete model. Our analysis shows that S_{bl} and S_{mo} vary with position and orientation of human during human movement.

E. Derivation of RSS-Based Intrusion Detection Bound Model

We show how to derive the bound for two typical detection methods based on FFT and wavelet transform. It should be noted that we will further propose two new methods in Section IV.B.

When there is no intruder, the RSS is denoted as $rss_0(t)$; when detecting an intruder, the RSS value is denoted as $rss_d(t)$. $rss_0(t)$ and $rss_d(t)$ can be derived according to equation (10). We first perform FFT on $rss_0(t)$ and $rss_d(t)$ respectively:

$$\mathbf{FFT_s}(m) = \sum_{t=0}^{N-1} rss_0(t) e^{\frac{-j2\pi mt}{N}}, m \in [0, N-1], \tag{17}$$

$$\mathbf{FFT_d}(n) = \sum_{t=0}^{N-1} rss_d(t) e^{\frac{-j2\pi nt}{N}}, n \in [0, N-1]. \tag{18}$$

$\mathbf{FFT_s}(m)$ represents the m-th output result after fast Fourier transform, $\mathbf{FFT_d}(n)$ represents the n-th output result after fast Fourier transform, and N is the number of signal samples. Then we extract the maximum amplitude except the 0-frequency component: $M_s = \max(|\mathbf{FFT_s}[1:N-1]|)$, $M_d = \max(|\mathbf{FFT_d}[1:N-1]|)$. The threshold RSS_{th} of (1) is set to M_s.

For wavelet transform method, we first perform Discrete Wavelet Transform (DWT) on $rss_0(t)$ and $rss_d(t)$ respectively and extract detail coefficients: $\mathbf{DWT_s}^{(l)}$ and $\mathbf{DWT_d}^{(j)}$, where l and j represent the decomposition level of DWT respectively. Then we calculate the corresponding variance: $V_s = \mathrm{var}(\mathbf{DWT_s})$, $V_d = \mathrm{var}(\mathbf{DWT_d})$. The threshold RSS_{th} of (1) is set to V_s.

When the detected result meets the condition in (1), the corresponding d_{TP} is the bound. According to equation (10), the intrusion detection bound model is closely related to the blocked area and reflection area. During the intrusion process, according to equation (11), when calculating the blocked area, the projected area may be on both the east and south walls, or in specific situations, only on the east or south wall. Consequently, the corresponding equation for calculating the blocked area varies, thereby affecting the establishment of the intrusion detection bound model. Similarly, in accordance with equation (16), the reflection surface of a person may be on the front, left, right, or lateral side, leading to diverse equations for calculating the reflection area, and in turn, resulting in different expressions of intrusion detection bound model.

Due to factors such as multipath and noise affecting RSS data, the intrusion detection bound is very limited and it should be further extended. Therefore, we next present effective methods to extend the intrusion detection bound. The specific process will be discussed in Section IV.

IV. Extending the Bound of Intrusion Detection

In this section, we first propose a performance indicator called R-ratio to extend the intrusion detection bound with RSS, and then present two new methods for to further extend the sensing bound.

A. The Definition of R-Ratio

Expanding $|H(f,t)|^2$ in equation (10), we can get :

$$\begin{aligned} |H(f,t)|^2 = {A_{noise}}^2 \Big(& |a_s(f)|^2 + |S_{mo}(f,t)|^2 \\ & + |S_{bl}(f,t)|^2 + |a_\varepsilon(f,t)|^2 + \\ & + 2\,|a_s(f) S_{mo}(f,t)| \cos\phi_{mos}(t) \\ & - 2\,|a_s(f) S_{bl}(f,t)| \cos\phi_{bls}(t) \\ & + 2\,|a_s(f) a_\varepsilon(f,t)| \cos\Delta\phi_{\varepsilon s} \\ & - 2\,|S_{bl}(f,t) S_{mo}(f,t)| \cos\phi_{blmo}(t) \\ & + 2\,|a_\varepsilon(f,t) S_{mo}(f,t)| \cos\phi_{mo\varepsilon}(t) \\ & - 2\,|a_\varepsilon(f,t) S_{bl}(f,t)| \cos\phi_{bl\varepsilon}(t) \Big), \end{aligned} \tag{19}$$

where $S_{bl}(f,t) = S_{bl}(t)\Gamma_{bl} a_{bl}(f,t)$ corresponds to the dynamic component blocked by human body, $S_{mo}(f,t) = S_{mo}(t)\Gamma_{mo} a_{mo}(f,t)$ corresponds to the dynamic component reflected by human body. We have also $\phi_{bls}(t) = \frac{2\pi d_{bl}(t)}{\lambda} -$

ϕ_s, $\phi_{mos}(t) = \frac{2\pi d_{mo}(t)}{\lambda} - \phi_s$, $\phi_{blmo}(t) = \frac{2\pi d_{mo}(t) - 2\pi d_{bl}(t)}{\lambda}$, $\phi_{bl\varepsilon}(t) = \frac{2\pi d_{bl}(t)}{\lambda} - \phi_\varepsilon$, and $\phi_{mo\varepsilon}(t) = \frac{2\pi d_{mo}(t)}{\lambda} - \phi_\varepsilon$.

In reality, apart from measurement noise, RSS readings in commodity WiFi devices contain impulse noise in amplitude and random offset in phase. As mentioned in reference [41], the impulse noise is caused by the internal state changes in WiFi devices, e.g, transmission rate adaptation and transmission power adaptation. Within a short period of time (e.g. 5 ms between two adjacent RSS readings, if RSS sampling rate is 200 Hz), the internal state of WiFi devices seldomly changes, and the impulse noise can be regarded to be constant in amplitude. All of these factors contribute to the RSS abnormal variation.

To alleviate the impact of impulse noise on the amplitude, we divide the RSS at time t by the RSS at time t_0. Then, the RSS ratio (R-ratio) is defined as follows:

$$R = \frac{|H(f,t)|^2 \times P_t}{|H(f,t_0)|^2 \times P_t} = \frac{|H(f,t)|^2}{|H(f,t_0)|^2}. \tag{20}$$

The R of (20) represents a normalized measure of the change in RSS over time. Substituting (19) into (20), we can get (21).

$$R = \frac{|a_s(f)|^2 + N_1(f,t) - N_2(f,t) + N_3(f,t) + N_4(f,t)}{|a_s(f)|^2 + N_1(f,t_0) - N_2(f,t_0) + N_3(f,t_0) + N_4(f,t_0)} \tag{21}$$

where

$$N_1(f,t) = |S_{mo}(f,t)|^2 + |S_{bl}(f,t)|^2 + |a_\varepsilon(f,t)|^2, \tag{22}$$

$$N_2(f,t) = 2\,|S_{bl}(f,t)S_{mo}(f,t)| \cos\phi_{blmo}(t), \tag{23}$$

$$N_3(f,t) = 2|a_s(f)|(|S_{mo}(f,t)| \cos\phi_{mos}(t) - |S_{bl}(f,t)| \cos(\phi_{bls}(t)) + |a_\varepsilon(f,t)| \cos\Delta\phi_{\varepsilon s}), \tag{24}$$

$$N_4(f,t) = 2\,|a_\varepsilon(f,t)|\,(|S_{mo}(f,t)| \cos\phi_{mo\varepsilon}(t) - |S_{bl}(f,t)| \cos\phi_{bl\varepsilon}(t)). \tag{25}$$

A relatively stable indoor environment in which the building structure and object layout are relatively unchanged is usually common in real life, especially in a home environment where owners are typically absent during working hours. In this scenario, it can be considered that the relatively static building structure and object layout will dominate the static components in the intrusion detection system, the noise component and dynamic component are normally much smaller than the static component. So we can ignore the $N_1(f,t)$, $N_2(f,t)$, $N_4(f,t)$, $N_1(f,t_0)$, $N_2(f,t_0)$, $N_4(f,t_0)$ components in the numerator and denominator. Then, equation (21) can be rewritten as:

$$R \approx \Bigg(|a_s(f)|^2 + 2|a_s(f)|\,(|S_{mo}(f,t)| \cos\phi_{mos}(t) - |S_{bl}(f,t)| \cos\phi_{bls}(t) + |a_\varepsilon(f,t)| \cos\Delta\phi_{\varepsilon s})\Bigg) \Bigg/ \Bigg(|a_s(f)|^2 + 2|a_s(f)|\,(|S_{mo}(f,t_0)| \cos\phi_{mos}(t_0) - |S_{bl}(f,t_0)| \cos\phi_{bls}(t_0) + |a_\varepsilon(f,t_0)| \cos\Delta\phi_{\varepsilon s})\Bigg) \tag{26}$$

Then, we extract $|a_s(f)|^2$ in the denominator of (26) to prepare for its subsequent transformation into the form of Taylor series expansion, so (26) can be rewritten as:

$$R \approx \Bigg(|a_s(f)|^2 + 2|a_s(f)|\,(|S_{mo}(f,t)| \cos\phi_{mos}(t) - |S_{bl}(f,t)| \cos\phi_{bls}(t) + |a_\varepsilon(f,t)| \cos\Delta\phi_{\varepsilon s})\Bigg) \Bigg/ \Bigg(|a_s(f)|^2\,(1 + 2|a_s(f)|(|S_{mo}(f,t_0)| \cos\phi_{mos}(t_0) - |S_{bl}(f,t_0)| \cos\phi_{bls}(t_0) + |a_\varepsilon(f,t_0)| \cos\Delta\phi_{\varepsilon s})/|a_s(f)|^2)\Bigg) \tag{27}$$

When the intrusion is detected at t but not at t_0, it can be regarded that there is no dynamic component at time t_0, then (27) can be rewritten as:

$$R \approx \Bigg(|a_s(f)|^2 + 2|a_s(f)|\,(|S_{mo}(f,t)| \cos\phi_{mos}(t) - |S_{bl}(f,t)| \cos\phi_{bls}(t) + |a_\varepsilon(f,t)| \cos\Delta\phi_{\varepsilon s})\Bigg) \Bigg/ |a_s(f)|^2\left(1 + 2|a_s(f)a_\varepsilon(f,t_0)| \cos\Delta\phi_{\varepsilon s}/|a_s(f)|^2\right) \tag{28}$$

Since the noise component is smaller than the static component, $2|a_s(f)a_\varepsilon(f,t_0)| \cos\Delta\phi_{\varepsilon s}$ is much smaller than $|a_s(f)|^2$. Therefore, we can truncate the Taylor series expansion of the denominator and keep only the first two terms as $1 - \frac{2|a_s(f)a_\varepsilon(f,t_0)| \cos\Delta\phi_{\varepsilon s}}{|a_s(f)|^2}$. The dynamic component and noise component are smaller than the static component, so $2|a_s(f)S_{mo}(f,t)| \cos\phi_{mos}(t)$ and $2|a_s(f)a_\varepsilon(f,t)| \cos\Delta\phi_{\varepsilon s}{}'$ are smaller than $|a_s(f)|^2$. Put $1 - \frac{2|a_s(f)a_\varepsilon(f,t_0)| \cos\Delta\phi_{\varepsilon s}}{|a_s(f)|^2}$ into equation (28), we can obtain:

$$R \approx \frac{2\,|S_{mo}(f,t)| \cos\phi_{mos}(t)}{|a_s(f)|} - \frac{2\,|S_{bl}(f,t)| \cos\phi_{bls}(t)}{|a_s(f)|} + \frac{2\,|a_\varepsilon(f,t)| \cos\Delta\phi_{\varepsilon s}}{|a_s(f)|} - \frac{|a_s(f)|}{|a_s(f)|}\frac{2\,|a_\varepsilon(f,t_0)| \cos\Delta\phi_{\varepsilon s}}{|a_s(f)|}. \tag{29}$$

We mark $2|a_\varepsilon(f,t)| \cos\Delta\phi_{\varepsilon s} - 2|a_\varepsilon(f,t_0)| \cos\Delta\phi_{\varepsilon s}$ as $|a_\varepsilon(f,t)'|$, so equation (29) can be rewritten as:

$$R \approx \underbrace{\frac{2\,|S_{mo}(f,t)| \cos\phi_{mos}(t)}{|a_s(f)|}}_{\mathrm{I}} \underbrace{- \frac{2\,|S_{bl}(f,t)| \cos\phi_{bls}(t)}{|a_s(f)|}}_{\mathrm{II}} + \underbrace{\frac{|a_\varepsilon(f,t)'|}{|a_s(f)|}}_{\mathrm{III}}. \tag{30}$$

The newly constructed RSS ratio signal has three parts: I corresponds to the dynamic part of human body reflection; II corresponds to the dynamic part of human body blocked; III corresponds to noise. According to the above equation, the impulse noise on amplitude is mitigated, but the measurement noise is not completely removed, which enlightens us to design a filter in next subsection to suppress the measurement noise.

B. Designing a Filter to Reduce Measurement Noise

From equation (30), we observe that the measurement noise is not completely removed. To effectively remove this measurement noise, we exploit the statistical properties of noise. The measurement noise follows a complex Gaussian distribution with zero mean and a variance of $\sigma^2(f)$ and its amplitude follows a Rayleigh distribution. Therefore, we design a Rayleigh filter to suppress measurement noise. The core of Rayleigh filter involves a weighted averaging of the entire signal to mitigate measurement noise. In this process, data points closer to the peak of the signal have a greater impact, receiving higher weights, while points farther away exert less influence and consequently receive reduced weights. The selection of weights for the Rayleigh filter is guided by the shape of the Rayleigh function. Due to the shape of the Rayleigh function, the peak points of the signal will be more strongly enhanced, while noise or low-amplitude signals will be suppressed. The one-dimensional Rayleigh probability density function is:

$$f(x) = \frac{x}{\sigma^2} e^{-\frac{x^2}{2\sigma^2}}, x \geq 0, \tag{31}$$

where x is the measurement noise amplitude, σ is the scale parameter of the Rayleigh function, which is related to the shape and peak position of the Rayleigh function. The Rayleigh function (31) illustrates a right-skewed waveform, with its peak occurring in the positive part. Hence, when designing the Rayleigh template, the size is usually considered to at least cover the peak area of the Rayleigh function. Specifically, when x equals σ, the Rayleigh function value is maximum, so the size of the Rayleigh template we designed must be at least larger than σ. The size of the Rayleigh template designed in this article is $r(r > \sigma)$. To obtain specific weight coefficients, the Rayleigh function needs to be discretized. During discretization, the curve of the Rayleigh function can be sampled, and the obtained discrete Rayleigh function value can be used as the coefficient of the Rayleigh template. Subsequently, the mathematical expression of each weight coefficient value in the Rayleigh template is given by:

$$w(i) = \frac{i-1}{\sigma^2} e^{-\frac{(i-1)^2}{2\sigma^2}}, i = 1, 2, \ldots r, \tag{32}$$

where $w(i)$ is the i-th weight coefficient value in the template.The weights are normalized to sum to 1:

$$normal_w(i) = \frac{w(i)}{\sum_i^r w(i)}, i = 1, 2 \ldots r. \tag{33}$$

When applying this proposed Rayleigh template to the corresponding noise data, a convolution operation is usually used.

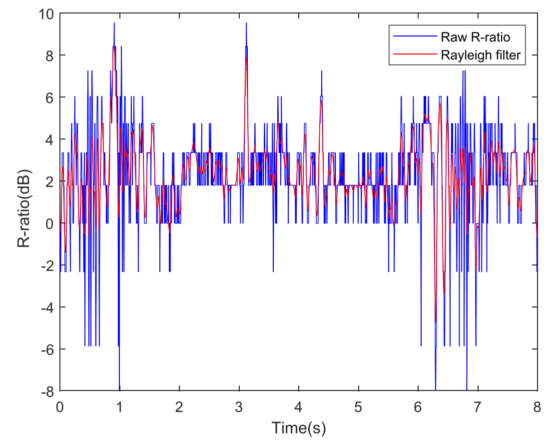

Fig. 7. R-ratio denoising.

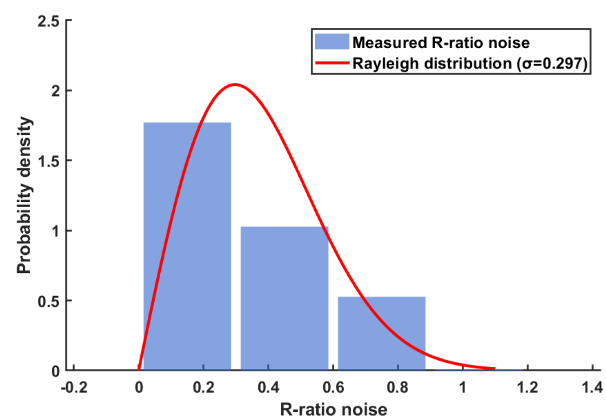

Fig. 8. Comparison of measured R-ratio noise and Rayleigh distribution.

The specific mathematical form is as follows:

$$R(t) = \begin{bmatrix} R(m) \\ \cdots \\ R(t) \\ \cdots \\ R(n) \end{bmatrix}^T \begin{bmatrix} normal_w(1) \\ \cdots \\ normal_w\,(max\_index) \\ \cdots \\ normal_w(r) \end{bmatrix}, \tag{34}$$

where $m = t - max_{index} + 1$, $n = t + r - max_{index}$, and $max_{index} = \arg\max(\mathbf{normal_w})$, representing the index of the maximum value in the weight. Fig. 7 illustrates the results of denoised R-ratio data through the proposed Rayleigh filter. Convolve the data to be processed with the designed Rayleigh template. And ensure that the key parts of the signal during the convolution process are aligned with the position of the maximum weight coefficient in the template. Through this process, we can successfully obtain denoised data.

We compare the experimental data with Rayleigh probability density function (PDF) in Fig. 8, where the histogram represents the R-ratio noise PDF and the red curve represents the theoretical Rayleigh distribution. The R-ratio noise is obtained when there is no intruder. As shown in Fig. 8, the R-ratio noise is consistent with the Rayleigh distribution.

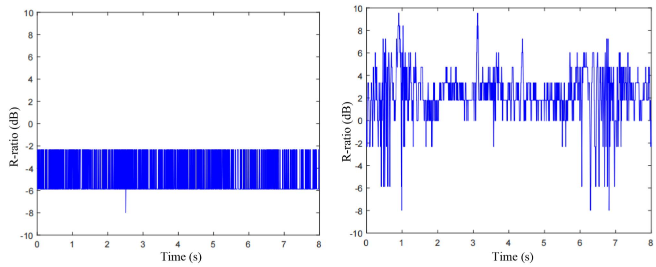

(a) No-intruder scenario (b) Intruder scenario

Fig. 9. R-ratio variation.

C. Two New Methods for Extending Intrusion Detection Bound

In our designed WiFi sensing system, the intrusion detection bound represents the maximum distance at which intruders can be reliably detected. We propose two new methods for extending intrusion detection bound. The two new methods make significant improvement on the existing FFT-based method and wavelet-based method.

1) Improved Intrusion Detection Method Based on Frequency-Domain Power Sum Ratio: In a typical indoor environment, due to multipath effects, environmental factors and noise interference, R-ratio may still exhibit fluctuation even in the absence of human movement. Fig. 9(a) illustrates the variation of R-ratio in a static environment, while Fig. 9(b) depicts the fluctuation of R-ratio caused by human intrusion. From Fig. 9, we can find different fluctuation patterns occur in static and intrusion environment. Particularly, during human movement, the signal waveform demonstrates rapid changes with specific frequency components. To deal with this challenge, we propose to use Fourier transform (FFT) to perform frequency domain analysis on the R-ratio signal data. And we analyze the changes in R-ratio in the frequency domain to complete the detection of human intrusion motion. The WiFi works at 5.24 GHz and the sampling frequency is set to 200 Hz, providing sufficient capability to capture the frequency changes associated with the human body movements.

Traditional methods typically emphasize the DC component of the signal, corresponding to the amplitude value at 0 Hz frequency. In signal processing, the 0-frequency component corresponds to the DC component of the signal, which is equal to the mean or offset value of the signal. The DC component usually represents the average level of the signal. However, in the intrusion scenario, we pay more attention to the dynamic changes of the signal caused by human movement, rather than solely on the overall average level. Therefore, we propose an improved FFT method that considers power sum ratio of the single-sided spectrum except the 0-frequency component. The improved FFT method is illustrated as follow.

We first apply fast Fourier transform to the R-ratio data over a time window. Since signals are real, and positive and negative frequencies are conjugate symmetric, we use half of the spectral length, as dropping the negative frequencies does not lead to any information loss. So we calculate the single-sided spectrum. The amplitudes in the original spectrum need to be scaled to maintain the total energy of the signal. Specifically, we double the amplitude of frequency components except the DC component and the Nyquist frequency, and obtain the single-sided spectrum.

Then we define power sum ratio of the single-sided spectrum and use it as a key feature for intrusion detection. The power sum ratio is defined as the percentage of the total power in a certain frequency range (0, f_{max}] with respect to the total power in whole band of the above single-sided spectrum. It can be calculated as:

$$PSR = \frac{\sum_{n=1}^{N \cdot f_{max}} |\mathbf{FFT_d}(n)|^2}{\sum_{n=0}^{N} |\mathbf{FFT_d}(n)|^2} \tag{35}$$

where F_s is the RSS sampling rate. f_{max} can be set to 10Hz, according to the analysis in [42].

If the power sum ratio is larger than the detection threshold, the intrusion is detected. The threshold should be automatically calculated and adapt to the environment. Although an easy way to set the threshold is setting it to be power sum ratio in any one time window in static environment, it easily causes false intrusion detection due to the varying power sum ratio in different time windows even in static environment. To avoid false intrusion detection, the threshold is automatically calculated as the maximum power sum ratio over multiple time windows in static environment.

The superiority of our proposed power sum ratio over frequency-domain amplitude peak is shown by preliminary experiment results as Fig. 10. The single-sided spectrum of R-ratio data over a time window in the no-intruder scenario is presented in Fig. 10(a), while the single-sided spectrum over the current time window in the intruder scenario is presented in Fig. 10(b). The amplitude peak in intruder scenario is 0.392, smaller than the maximum amplitude peak in no-intruder scenario which is 0.414, probably because the intruder is as far as 7 m away from the transmitter. In this case, the intrusion cannot be detected by frequency-domain amplitude peak. However, our proposed power sum ratio can avoid the above misdetection. As shown in Fig. 10(a), the power sum ratio in the single-sided spectrum is 52.6%, while the power sum ratio in intruder scenario is 71.47% as shown in Fig. 10(b). Obviously, the power sum ratio in intruder scenario is larger than the maximum power sum ratio in no-intruder scenario, so the intrusion can be successfully detected.

2) Improved Intrusion Detection Method Based on Scale Projection Wavelet Transform: Since the human motion speed vary among individuals or for the same person at different times, we need a technique that can provide variable frequency resolution. Compared to other techniques, wavelet analysis provides both time and frequency locality at different resolutions as well as being computationally efficient. Hence, we propose an improved wavelet transform method for intrusion detection. In wavelet transform, detail coefficients typically contain local features in the signal which accurately capture characteristics associated with intrusion. In intrusion detection, choosing the appropriate level of decomposition is crucial. Lower decomposition levels may fail to capture information at the frequency of human motion, while higher decomposition levels may bring noise or unnecessary details. Therefore, it is particularly necessary to

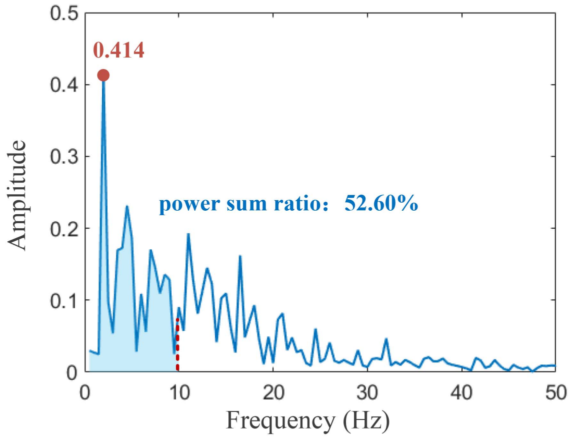

(a) power sum ratio in no-intruder scenario

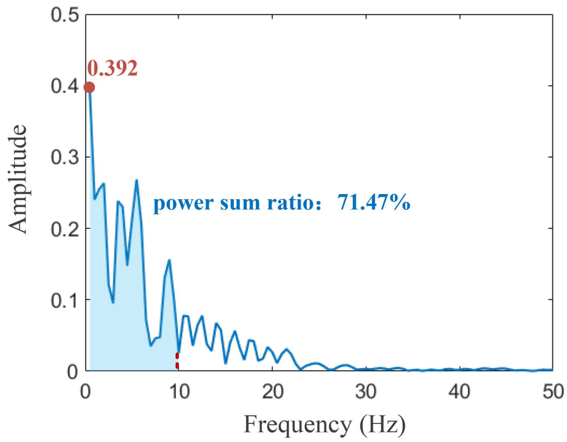

(b) power sum ratio in intruder scenario

Fig. 10. Spectrum of the R-ratio data over a time window 0.5 s.

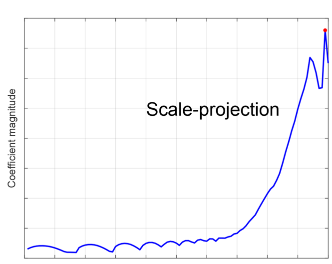

(a) Coefficient magnitude

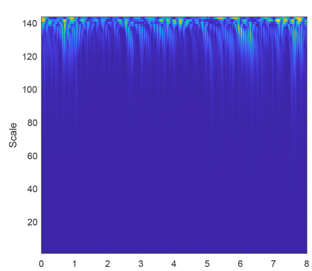

(b) Scale

Fig. 11. Detecting frequencies of interest dynamically using scale projection.

select the level of decomposition based on the the frequency of human motion. In this paper, we proposes a method to identify the frequency of human motion based on scale projection.

Specifically, we leverage a wavelet-based denoising method for further refinement. The method based on scale projection identifies the main frequency we are interested in from the wavelet transform spectrogram, as shown in Fig. 11. The scale projection technique projects the spectrogram on the y-axis (i.e. the scale axis), maintaining the maximum value for each projected row. Then, it extracts the top local-maximums values:$\{(s_1, c_1), (s_2, c_2), (s_3, c_3), \ldots\ldots, (s_k, c_k)\}$,

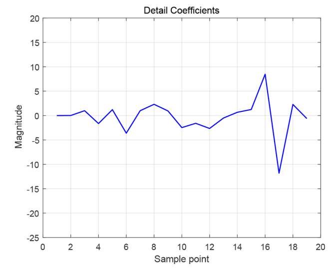

(a) No-intruder scenario

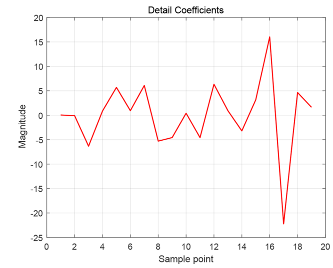

(b) Intruder scenario

Fig. 12. Detail coefficients.

where (s_i, c_i) is the i-th top scale and projected coefficient value at that scale, respectively. The scale of interest is estimated as:

$$s^* = s\left(\arg\max\left(c_i\right)\right), \text{s.t.} i = 1, \ldots k. \tag{36}$$

After obtaining the scale information, according to the relationship between scale and frequency, we can get the frequency we are interested in: $f = \frac{F_s * f_{wc}}{s^*}$, where f_{wc} is the center frequency of wavelet. Subsequently, based on the identified frequency of interest, we can selectively choose an appropriate level of decomposition to extract detail coefficients associated with specific motion frequencies. This process allows us to focus on signal features within the target frequency range, facilitating a more precise capture information relevant to motion events.

Fig. 12(a) is the detail coefficient waveform in a no-intruder scenario, and Fig. 12(b) depicts the detail coefficient waveform in an intruder scenario. We can clearly observe that in the presence of human movement, the fluctuation of the detail coefficient is significantly higher than in a no-intruder environment. When the variance of the dynamic detail coefficient is greater than the maximum variance of static detail coefficient, an intrusion is detected.

D. Computational Complexity of Our Intrusion Detection Scheme

The computational complexity of our intrusion detection scheme consists of the complexity of R-ratio, Rayleigh filter and our improved intrusion detection method. The improved intrusion detection method is either based on frequency-domain power sum ratio, or based on scale projection wavelet transform. Either method is more complex than R-ratio and Rayleigh filter, so the complexity of our intrusion detection scheme is mainly decided by our improved intrusion detection method. Without loss of the generality, we next analyze the complexity of the improved method based on frequency-domain power sum ratio. The calculation of power sum ratio is explained as follow: firstly performing FFT on the denoised R-ratio data over a time window, secondly summing up the power (represented by square of frequency-domain amplitude) in a certain frequency range, and thirdly calculating the percentage of the total power in above range with respect to the total power in whole frequency band. In the above process, FFT is the most complex, with the complexity of O(n∗log$n$). So the complexity of the improved method based on power sum ratio, as well as the complexity of our intrusion detection scheme, is O(n∗log$n$).

(a) Experiment scenario in the corridor

(b) Experiment scenario in the meeting room

Fig. 13. Experiment scenario.

TABLE I
EXPERIMENTAL SETUP

Parameter	Corridor	Meeting Room
Environment size	$15m \times 3m$	$8m \times 6m$
Antenna type	Omnidirectional	Omnidirectional
Distance between Tx and Rx	$1 \sim 3m$	$1 \sim 3m$
Orientation of the intruder	$0^\circ \sim 90^\circ$	$0^\circ \sim 90^\circ$
Signal frequency	5.24GHz	5.24GHz

V. EVALUATION

A. Evaluation Setup

To evaluate the system's ability to extend bound, we conduct real experiments in a corridor and a meeting room. The corridor is 3 meters wide and 15 meters long, while the meeting room is 6 meters wide and 8 meters long. The experimental scenario is shown in Fig. 13. We decrease the distance between the volunteer and transceiver from 10 m (corridor) or 8 m (meeting room) to 1 m. At every 1 m location, the volunteer walks back and forth for 8 seconds. As described in Table I, we use commercial Intel 5300 WiFi devices equipped with omnidirectional antenna to collect RSS data. The frequency is set to 5.24 GHz, bandwidth to 20 MHz and the transmitter sends 200 packets per second. The distance between Tx and Rx changes from 1 m to 3 m, while the orientation of the intruder toward WiFi device changes from 0° to 90°. To evaluate the system's intrusion detection range, we placed a series of tags on the ground to mark the distance to the WiFi devices. We have uploaded the code to the GitHub code repository, the link is as follows: https://github.com/5813gg/rss_intrude_code.

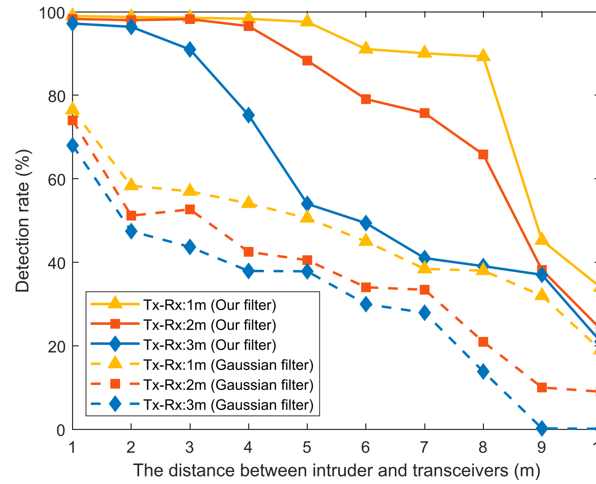

Fig. 14. The intrusion detection rates of our filter and Gaussian filter.

B. Performance in Intrusion Detection

Fig. 14 shows the detection performance of our filter and Gaussian filter. Here, intrusion detection rate is obtained as follow: we process the RSS data in each time window, determine whether the intrusion is detected or not in each time window, and calculate the ratio of intrusion-detected time windows to total time windows. Higher intrusion detection rate means higher possibility of successful intrusion detection. Fig. 14 demonstrates the contribution of our filter on improving the intrusion detection performance. Specifically, in the experiments, we first obtain detection rates by our power sum ratio based intrusion detection method which employs our filter to mitigate measurement noise, then we replace our filter by Gaussian filter and obtain intrusion detection rates again. As shown in Fig. 14, we can find that when the distance between the intruder and sensing device changes (as well as the Tx-Rx distance), the intrusion detection rates of our filter are always much higher than those of Gaussian filter. So, the experimental results demonstrate that our filter can effectively improve the intrusion detection performance.

Fig. 15 illustrates the detection performance of the improved intrusion detection method based on frequency-domain power sum ratio, with Fig. 15(a) showcasing the results based on raw RSS data and Fig. 15(b) presenting the results based on R-ratio. We can observe that as the distance increases, there is a gradual decrease in power sum ratio. In the case of raw data (Fig. 15(a)), when the distance extends to 5 meters, the power sum ratio falls below the threshold RSS_{th1}, establishing the perceptual bound at 4 meters. Conversely, for R-ratio data (Fig. 15(b)), when the distance reaches 9 meters, the power sum ratio drops below the threshold RSS_{th2}, resulting in a sensing bound of 8 meters. This observation shows that the data processing method based on R-ratio has the potential to double the sensing range compared to raw RSS data, highlighting its efficacy in enhancing detection performance at greater distances.

Then, we evaluate the wavelet transform method based on scale projection. We first perform intrusion detection on the raw RSS data, and subsequently, we perform intrusion detection on the R-ratio data. For the raw RSS data, the threshold (denoted as

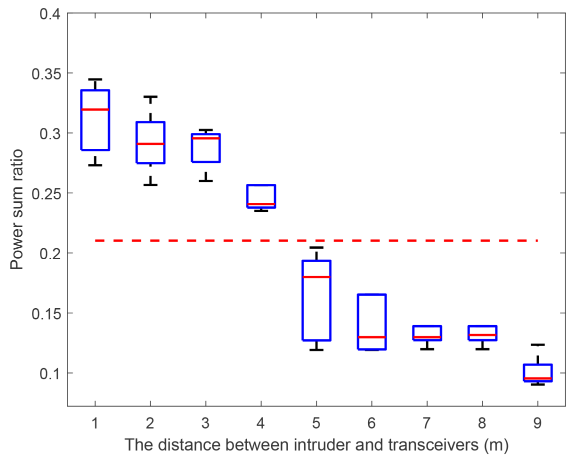

(a) Detection performance based on raw data

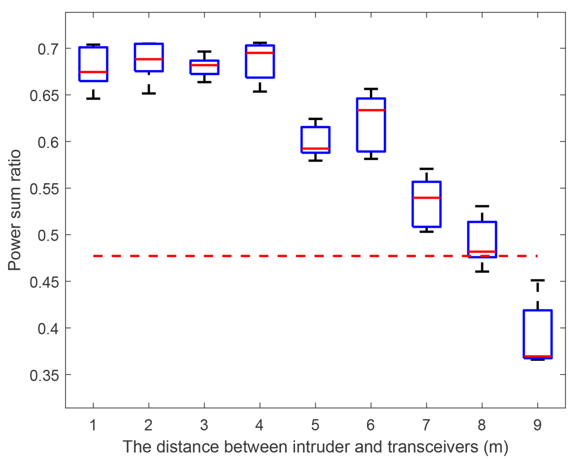

(b) Detection performance based on R-ratio

Fig. 15. Improved intrusion detection method based on frequency-domain power sum ratio.

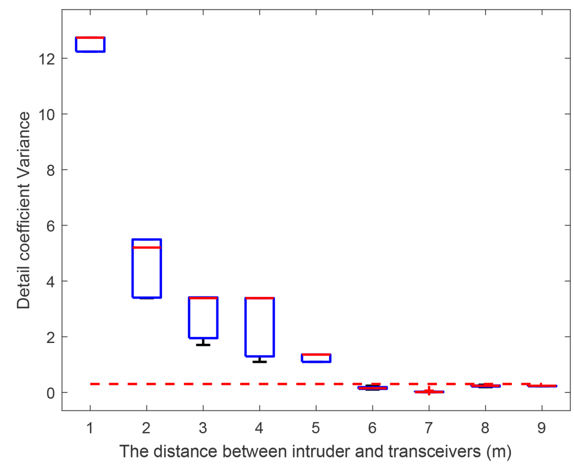

(a) Detection performance based on raw data

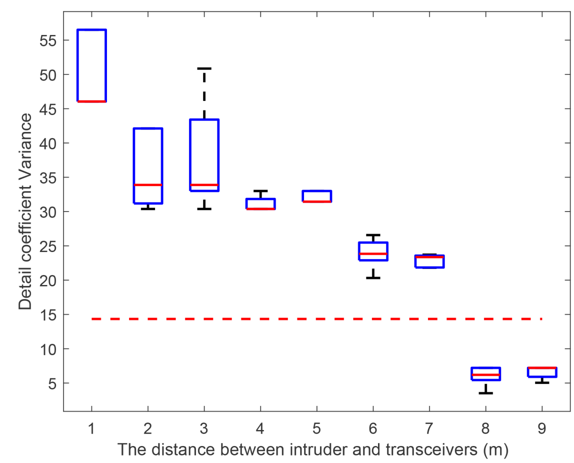

(b) Detection performance based on R-ratio

Fig. 16. Improved intrusion detection method based on scale projection wavelet transform.

RSS_{th3}) is determined as the variance of the detail coefficient processed by the improved wavelet transform of the RSS data in a static environment. When the RSS data in the intrusion environment surpasses RSS_{th3}, it is interpreted as an intrusion. Similarly, for R-ratio data, the threshold (denoted as RSS_{th4}) is established as the variance of the detail coefficient processed by the improved wavelet transform of the R-ratio data in a static environment. Detection of intrusion occurs when the R-ratio data in the intrusion environment exceeds RSS_{th4}.

Fig. 16 illustrates the detection performance of the improved wavelet transform method based on scale projection, with Fig. 16(a) presenting the results based on raw RSS data and Fig. 16(b) showcasing outcomes based on R-ratio. We can observe that as the distance increases, there is a gradual decrease in the variance of the detail coefficient. For raw data (Fig. 16(a)), when the distance extends to 6 meters, the variance of the detail coefficient falls below the threshold, establishing the intrusion detection bound at 5 meters, as depicted in the figure. Similarly, for R-ratio data (Fig. 16(b)), when the distance reaches 8 meters, the variance of the detail coefficient drops below the threshold, resulting in an intrusion detection bound of 7 meters. Combined with Fig. 15(a) and (b), experiments results show that the data processing method based on R-ratio can extend the sensing range.

C. Comparison With Existing Work

The proposed RSS model has been compared with measured RSS data and knife-edge diffraction-based RSS model [43]. We utilized the Kolmogorov-Smirnov (KS) test to calculate the KS statistic. This statistic represents maximum vertical distance between empirical cumulative distribution function and theoretical cumulative distribution function. The KS statistic measures goodness-of-fit between empirical and theoretical distributions, with smaller values indicating better similarity. The comparative cumulative distribution functions are presented for human intrusion detection ranges of 4 m, 6 m and 8 m, as shown in Fig. 17.

Fig. 17(a) presents the KS test results at 4-meter distance, where our model achieves a KS statistic of 0.071, smaller than the KS statistic of knife-edge model which is 0.924, demonstrating better similarity with the empirical CDF of measured RSS data. This performance advantage becomes more pronounced

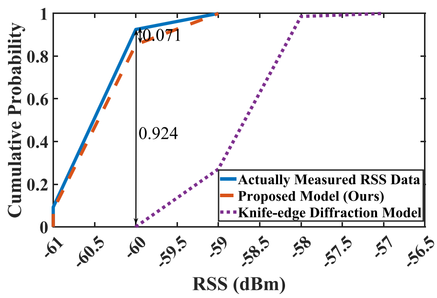

(a) The distance between intruder and transceivers (4-meter)

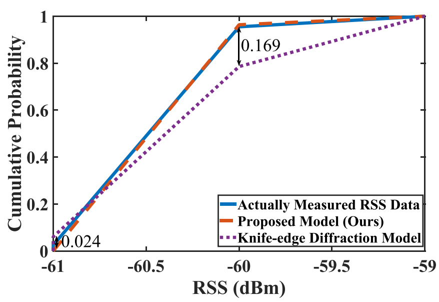

(b) The distance between intruder and transceivers (6-meter)

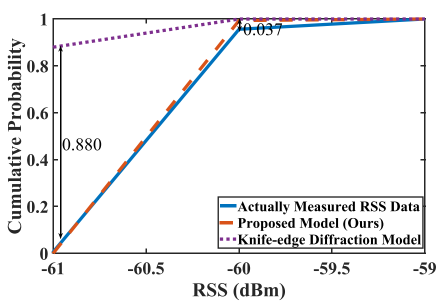

(c) The distance between intruder and transceivers (8-meter)

Fig. 17. KS test results at various human intrusion distance.

with increasing distance. As shown in Fig. 17(b), at 6-meter distance our model maintains a KS statistic of 0.024 while the knife-edge model exhibits a much larger KS statistic. The trend continues in Fig. 17(c) at 8-meter distance, where our model sustains a KS statistic of 0.037 while the knife-edge model exhibits a KS statistic of 0.880. These results confirm the superior consistency of our model with measured RSS data.

We also compare our work with existing research on motion detection systems. Specifically, we analyze the differences between R-ratio-based FFT, R-ratio-based DWT, and three RSS-based motion detection systems: HAR-FFT [44], WiGest [19] and Simple-HomeFi [8].

As shown in Fig. 18, when the distance between an intruder and the transceiver exceeds 4 meters, the detection performance of the HAR-FFT method [44] declines significantly. In contrast, our proposed R-ratio-based FFT method can still maintain high detection accuracy at the same distance. The HAR-FFT method does not denoise the RSS data. When the distance

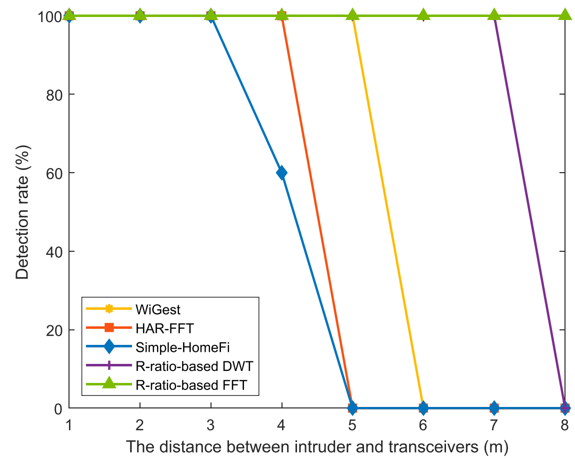

Fig. 18. Comparison between different methods.

between the intruder and the transceiver increases, the RSS variation becomes weaker and is more easily overwhelmed by impulse noise and measurement noise. Moreover, the HAR-FFT method employs simple feature extraction approach, as it extracts non-segmented frequency-domain features from the RSS data, namely, the amplitude of zero frequency of the RSSI data. However, the zero-frequency component normally represents the average level of the signal and fails to capture the details of signal variations caused by human motion. In contrast to the HAR-FFT method, we propose R-ratio to remove impulse noise. Additionally, measurement noise is mitigated through Rayleigh filtering. Furthermore, we propose an improved intrusion detection method based on frequency-domain power sum ratio. By the ratio of power within the human motion frequency band to the total frequency-domain power, our method significantly enhances the dynamic RSS variations induced by human motion. As a result, our method enables more sensitive detection of human intrusion.

The WiGest method [19] exhibits a significant decline in detection performance when the intruder is more than 5 meters away from the transceiver, whereas our proposed two methods maintain high detection accuracy at the same distance. Although the WiGest method uses DWT to denoise RSS data, it relies mainly on traditional time-frequency analysis, which cannot effectively mitigate impulse noise and capture the subtle dynamic features introduced by human motion. The discrete wavelet transform adopted by WiGest method uses a fixed decomposition level, unable to adapt to actual motion frequencies. In contrast to the WiGest method, our proposed method based on scale projection wavelet transform automatically identifies the dominant motion frequency through scale projection and dynamically selects the wavelet decomposition level, focusing feature extraction on the relevant frequency bands. As a result, our method significantly improves the efficiency of feature extraction and maintains high detection accuracy even at extended distances.

When the distance between an intruder and the transceiver exceeds 3 meters, the detection performance of the Simple-HomeFi method [8] declines sharply. The reason is that the

TABLE II
BODY SIZE PARAMETER TABLE OF DIFFERENT VOLUNTEERS

Volunteers	Gender	Height(cm)	Width(cm)	Length(cm)
1	male	178	25	45
2	male	178	25	40
3	male	170	20	40
4	female	168	15	30
5	female	160	15	30
6	female	155	15	25

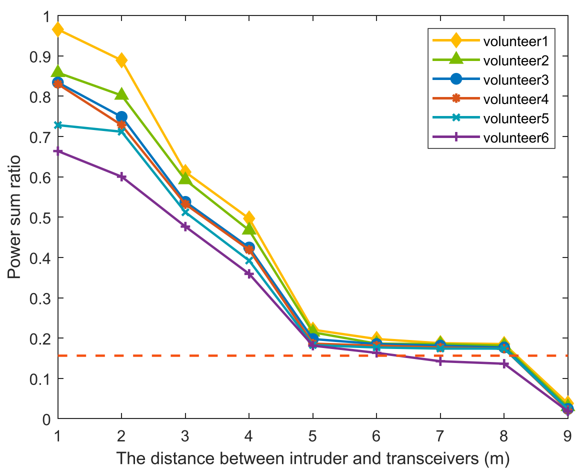

Fig. 19. Comparison between volunteers with different body sizes.

Simple-HomeFi method adopts the variance of RSS data to detect human intrusion, but the variance only represents the overall fluctuation of signal strength and cannot capture the subtle dynamic variations caused by human motion. In indoor environments, RSS fluctuations are caused by multiple factors such as multi-path effects, device noise and human movement. Sole dependence on the variance of RSS is unable to accurately identify true intrusion behaviors. In contrast to the Simple-HomeFi method, our proposed method based on scale projection wavelet can separate detailed components in different frequency bands and highlight dynamic changes related to human motion. Furthermore, our proposed method based on frequency-domain power sum ratio can effectively extract weak frequency-domain features of human movement at long distances, thereby achieving superior performance.

D. Impact of Intruders With Different Body Sizes

From equation (9), it becomes evident that human body sizes play a significant role in influencing RSS, consequently impacting the bound. In our experiment, we purposefully recruited six volunteers with diverse body sizes, comprising three men and three women. The body size details of these participants are presented in Table II. We use the improved FFT method based on power sum ratio for intrusion detection.

As illustrated in Fig. 19, with an increase in detection distance, the power sum ratio of each volunteer exhibits a decline. This phenomenon is attributed to indoor signal propagation losses caused by signal attenuation and multipath effects. In addition, larger-sized volunteers tend to exhibit higher power sum ratio.

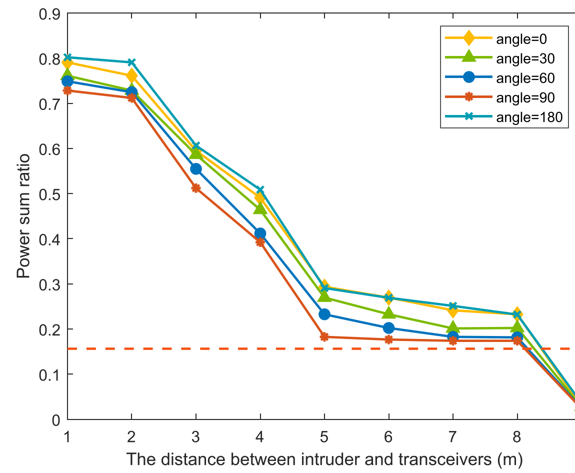

Fig. 20. Comparison between different angles.

For example, Volunteer 1, being the largest, has a larger reflection area, leading to a more extensive blocked area and a more pronounced impact on RSS. Consequently, intrusion motion can be detected at a position as far as 8 meters. In contrast, Volunteer 6, with the smallest body size, has a relatively smaller reflection area, resulting in a less conspicuous impact on RSS. As a result, intrusion motion can only be detected at a position of 6 meters.

According to the (11) and (16), both the blocked area and reflected area are intricately linked to human body size, exerting a direct influence on RSS. Consequently, when developing an intrusion detection system, careful consideration must be given to the placement of the WiFi transceiver. It involves factors such as choosing the height, angle, and orientation of the antenna, as well as formulating an overall placement strategy for the device.

E. Impact of Angle Between the Person and the WiFi Link

According to equation (10), the angle between the person and the WiFi link also has a significant impact on RSS. Therefore, in our experiment, we invited one of the volunteers to pose at various angles: 0 degrees (directly facing the WiFi link), 30 degrees, 60 degrees, 90 degrees, and 180 degrees (facing away from the WiFi link). To perform intrusion detection, We use the improved FFT method based on power sum ratio.

As depicted in Fig. 20, there is a noticeable decrease in power sum ratio at each angle as the detection distance increases. And larger angles correspond to smaller power sum ratio. The impact of volunteers on RSS is more pronounced at 0 degrees compared to 90 degrees, primarily because, at 0 degrees, both the reflected and blocked areas of the human body are larger, leading to a more conspicuous effect on RSS. Interestingly, the effects at 0 degrees and 180 degrees are nearly identical due to the equal front and back areas of the human body, resulting in similar reflected and blocked areas. The experiment revealed that when a person moves directly towards the WiFi link (0 degrees), the reflected and blocked areas of the human body are more extensive, significantly influencing RSS. Consequently, in the design of an intrusion detection system, strategic placement of the WiFi transceiver facing people can be considered to amplify

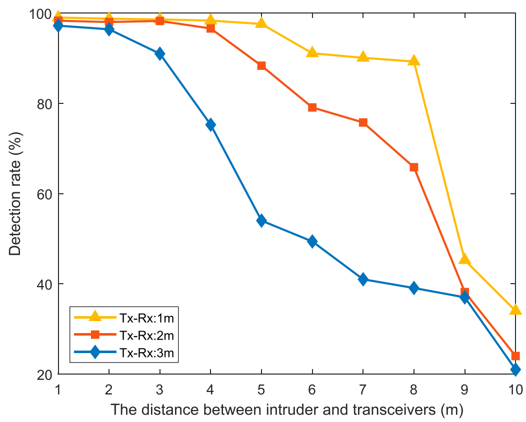

(a) Detection performance in the corridor

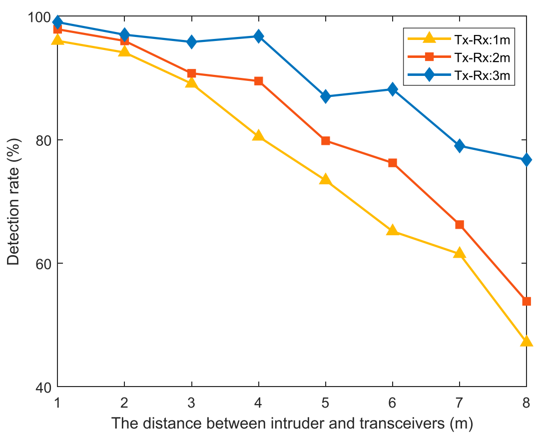

(b) Detection performance in the meeting room

Fig. 21. Comparison between different scenarios.

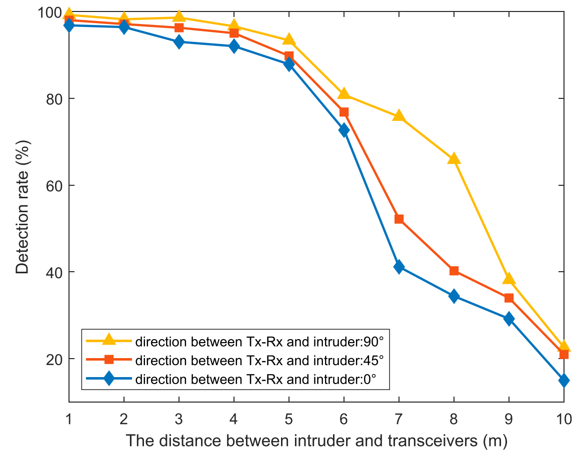

Fig. 22. Comparison between different transceiver locations.

changes in RSS signals, facilitating the detection of intrusion events.

Overall, the derived equation offers valuable insights and initial guidance regarding the influence of intruder size and angle on RSS. However, the precise placement of WiFi transceivers and the fine-tuning of system parameters demand more comprehensive and in-depth research and verification. Future research can further optimize the model and algorithm based on this paper to better adapt to the needs of intrusion detection under various environmental conditions.

F. Impact of Different Scenarios and Transceiver Locations

To further compare the performance in different environments, we conduct experiments in two typical scenarios: corridor and meeting room. In each scenario, the distance between the transmitter and receiver is set to 1 m, 2 m and 3 m. As shown in the Fig. 21, in the corridor, when the transceiver spacing is 1 m, the intrusion detection range corresponsding to 90% detection rate is long as 8 m. In contrast, in the conference room environment, when the distance between transceivers is 1 m, the intrusion detection range corresponsding to 90% detection rate is only 3 m. The reason is explained as follow. The corridor is an open space with few obstacle, while the meeting room has many obstacles such as desks and chairs. Due to fewer multipath reflection, the static signal component in the corridor is weaker than that in the meeting room. So it is easier to detect the dynamic component in the corridor than in the meeting room, resulting in longer intrusion detection range.

Next, we show the intrusion detection performance in different transceiver locations. The locations of Tx and Rx are rotated around the center point of Tx and Rx, thus the direction between Tx-Rx and intruder changes from 0° to 90°. The distance between Tx and Rx is kept at 2 m. As show in Fig. 22, when the transceivers change their locations, the direction between the line Tx-Rx and the intruder changes from 0° to 90°, the detection range corresponding to 90% detection rate is increased from 4.9 m to 5.2 m. The main reason is explained as follow. When the direction between Tx-Rx and intruder changes from 0° to 90°, according to the derivation of the reflection area and blocked area in RSS model in Section III, the human body reflects and blocks the signal in a larger area, making a more significant impact on the RSS. The greater impact on the RSS leads to larger variation of RSS, resulting in higher intrusion detection rate and longer intrusion detection range.

VI. Conclusion

In this article, to address the limitations of existing RSS-based intrusion detection solutions, we introduced a novel model of motion-disturbed RSS for improving the accuracy of the WiFi intrusion detection bound. The proposed R-ratio indicator served as an effective performance measure to extend this bound, taking into account the blocked and reflection areas within the motion-disturbed RSS model. Additionally, an efficient noise filter was designed to further enhance the system's robustness. We also provided two customized intrusion detection methods to evaluate the R-ratio performance. The experimental results demonstrated the superiority of the R-ratio-based intrusion detection method, showcasing an approximate doubling of the WiFi intrusion detection bound compared to other approaches utilizing raw RSS data. Furthermore, the proposed motion-disturbed RSS model offered valuable insights and guidance for enhancing the overall performance of intrusion detection systems. Limitations and future work: in more complex environments, LoS signal will be completely blocked, so NLoS scenarios with various obstacles will be investigated in future work. Besides, if the intruder sits there breathing, intrusion detection becomes challenging due to the relatively subtle changes in RSS. Future research will include the refinement of RSS signal model to achiev a good balance between its complexity and accuracy, the enhancement of the SNR of the RSS to improve detection accuracy and reliability, etc.

REFERENCES

[1] S. He, J. Chen, X. Li, X. Shen, and Y. Sun, "Mobility and intruder prior information improving the barrier coverage of sparse sensor networks," *IEEE Trans. Mobile Comput.*, vol. 13, no. 6, pp. 1268–1282, Jun. 2014.

[2] F. Viani, F. Robol, A. Polo, P. Rocca, G. Oliveri, and A. Massa, "Wireless architectures for heterogeneous sensing in smart home applications: Concepts and real implementation," *Proc. IEEE*, vol. 101, no. 11, pp. 2381–2396, Nov. 2013.

[3] Y. Wang, K. Wu, and L. M. Ni, "WiFall: Device-free fall detection by wireless networks," *IEEE Trans. Mobile Comput.*, vol. 16, no. 2, pp. 581–594, Feb. 2017.

[4] R. Nayak, M. M. Behera, U. C. Pati, and S. K. Das, "Video-based real-time intrusion detection system using deep-learning for smart city applications," in *Proc. 2019 IEEE Int. Conf. Adv. Netw. Telecommun. Syst.*, 2019, pp. 1–6.

[5] S. Klakegg et al., "Assisted medication management in elderly care using miniaturised near-infrared spectroscopy," *Proc. ACM Interact. Mob. Wearable Ubiquitous Technol.*, vol. 2, no. 2, pp. 1–24, Jul. 2018.

[6] W. Xu, Z. Yu, Z. Wang, B. Guo, and Q. Han, "AcousticID: Gait-based human identification using acoustic signal," *Proc. ACM Interact. Mob. Wearable Ubiquitous Technol.*, vol. 3, no. 3, pp. 1–25, Sep. 2019.

[7] S. Otoum, B. Kantarci, and H. T. Mouftah, "On the feasibility of deep learning in sensor network intrusion detection," *IEEE Netw. Lett.*, vol. 1, no. 2, pp. 68–71, Jun. 2019.

[8] Y. Jin, Z. Tian, M. Zhou, Z. Li, and Z. Zhang, "An adaptive and robust device-free intrusion detection using ubiquitous WiFi signals," in *Proc. IEEE 23rd Int. Conf. Digit. Signal Process.*, 2018, pp. 1–5.

[9] Z. Tian, Y. Li, M. Zhou, and Z. Li, "WiFi-based adaptive indoor passive intrusion detection," in *Proc. IEEE 23rd Int. Conf. Digit. Signal Process.*, 2018, pp. 1–5.

[10] J. Zhang, G. Song, G. Qiao, T. Meng, and H. Sun, "An indoor security system with a jumping robot as the surveillance terminal," *IEEE Trans. Consum. Electron.*, vol. 57, no. 4, pp. 1774–1781, Nov. 2011.

[11] A. E. Kosba, A. Abdelkader, and M. Youssef, "Analysis of a device-free passive tracking system in typical wireless environments," in *Proc. 3rd Int. Conf. New Technol.*, Mobility and Security, 2009, pp. 1–5.

[12] Y. Xie, Z. Li, and M. Li, "Precise power delay profiling with commodity Wi-Fi," *IEEE Trans. Mobile Comput.*, vol. 18, no. 6, pp. 1342–1355, Jun. 2019.

[13] Y. Zeng, D. Wu, R. Gao, T. Gu, and D. Zhang, "FullBreathe: Full human respiration detection exploiting complementarity of CSI phase and amplitude of WiFi signals," *Proc. ACM Interact. Mob. Wearable Ubiquitous Technol.*, vol. 2, no. 3, pp. 1–19, Sep. 2018.

[14] C. Wu, F. Zhang, Y. Hu, and K. J. R. Liu, "GaitWay: Monitoring and recognizing gait speed through the walls," *IEEE Trans. Mobile Comput.*, vol. 20, no. 6, pp. 2186–2199, Jun. 2021.

[15] J. Wang, Z. Tian, M. Zhou, J. Wang, X. Yang, and X. Liu, "Leveraging hypothesis testing for CSI based passive human intrusion direction detection," *IEEE Trans. Veh. Technol.*, vol. 70, no. 8, pp. 7749–7763, Aug. 2021.

[16] S. I. Shah, S. Y. Shah, and S. A. Shah, "Intrusion detection through leaky wave cable in conjunction with channel state information," in *Proc. 2019U.K./China Emerg. Technol.*, 2019, pp. 1–4.

[17] L. Gui, W. Yuan, and F. Xiao, "CSI-based passive intrusion detection bound estimation in indoor NLOS scenario," *Fundam. Res.*, vol. 3, no. 6, pp. 988–996, 2023.

[18] L. Gui, W. Yuan, and F. Xiao, "Blind-area elimination in video surveillance systems by WiFi sensing with minimum QoS loss," in *Proc. IEEE/ACM 30th Int. Symp. Qual. Serv.*, 2022, pp. 1–10.

[19] H. Abdelnasser, K. Harras, and M. Youssef, "A ubiquitous WiFi-based fine-grained gesture recognition system," *IEEE Trans. Mobile Comput.*, vol. 18, no. 11, pp. 2474–2487, Nov. 2019.

[20] Z. Dong, F. Li, J. Ying, and K. Pahlavan, "A model-based RF hand motion detection system for shadowing scenarios," *IEEE Access*, vol. 8, pp. 115662–115672, 2020.

[21] J. Wang, Q. Gao, M. Pan, X. Zhang, Y. Yu, and H. Wang, "Toward accurate device-free wireless localization with a saddle surface model," *IEEE Trans. Veh. Technol.*, vol. 65, no. 8, pp. 6665–6677, Aug. 2016.

[22] C. E. O'Lone, H. S. Dhillon, and R. M. Buehrer, "Characterizing the first-arriving multipath component in 5G millimeter wave networks: Toa, aoa, and non-line-of-sight bias," *IEEE Trans. Wireless Commun.*, vol. 21, no. 3, pp. 1602–1620, Mar. 2022.

[23] Y. He et al., "Modeling solar radiation on a human body indoors by a novel mathematical model," *Building Environ.*, vol. 187, 2021, Art. no. 107421.

[24] H. Yalduz, T. E. Tabaru, V. T. Kilic, and M. Turkmen, "Design and analysis of low profile and low sar full-textile UWB wearable antenna with metamaterial for WBAN applications," *AEU- Int. J. Electron. Commun.*, vol. 126, 2020, Art. no. 153465.

[25] A. Jabbar, M. Zubair, M. A. Naveed, M. Q. Mehmood, and Y. Massoud, "A photopaper-based low-cost, wideband wearable antenna for wireless body area network applications," *IET Microw., Antennas Propag.*, vol. 16, no. 15, pp. 962–970, 2022.

[26] L. Chen, J. Zou, M. Lan, Y. Zhao, and S. Ge, "Human body shadowing properties of the sub-6GHz electromagnetic-wave mainstream frequency band," *IEEE Access*, vol. 11, pp. 82108–82117, 2023.

[27] V. Rampa, G. G. Gentili, S. Savazzi, and M. D'Amico, "Em models for passive body occupancy inference," *IEEE Antennas Wireless Propag. Lett.*, vol. 16, pp. 2517–2520, 2017.

[28] V. Rampa, S. Savazzi, M. Nicoli, and M. D'Amico, "Physical modeling and performance bounds for device-free localization systems," *IEEE Signal Process. Lett.*, vol. 22, no. 11, pp. 1864–1868, Nov. 2015.

[29] F. Zhang et al., "Towards a diffraction-based sensing approach on human activity recognition," *Proc. ACM Interactive, Mobile, Wearable Ubiquitous Technol.*, vol. 3, no. 1, pp. 1–25, 2019.

[30] F. Zhang et al., "From Fresnel diffraction model to fine-grained human respiration sensing with commodity Wi-Fi devices," *Proc. ACM Interact. Mob. Wsearable Ubiquitous Technol.*, vol. 2, no. 1, pp. 1–23, Mar. 2018.

[31] Y. Zeng, D. Wu, J. Xiong, E. Yi, R. Gao, and D. Zhang, "FarSense: Pushing the range limit of WiFi-based respiration sensing with csi ratio of two antennas," *Proc. ACM Interact. Mob. Wearable Ubiquitous Technol.*, vol. 3, no. 3, pp. 1–26, Sep. 2019.

[32] S. Li et al., "WiBorder: Precise Wi-Fi based boundary sensing via through-wall discrimination," *Proc. ACM Interact. Mob. Wearable Ubiquitous Technol.*, vol. 4, no. 3, pp. 1–30, Sep. 2020.

[33] Y. Zhao, C. Ju, D. Wang, N. Liu, L. Guan, and P. Xie, "SNR estimation for 5G satellite-to-ground communication in ultra-low SNR environment based on channel frequency response reconstruction," *IEEE Commun. Lett.*, vol. 28, no. 2, pp. 357–361, Feb. 2024.

[34] T. S. Rappaport, *Wireless Communications: Principles and Practice*, 2nd ed. Noida, Uttar Pradesh, India: Pearson Educ. India, 2010.

[35] S. Zaravashan, S. Arefizadeh, and S. Torabi, "Efficient sub-carrier relationship extraction for human activity recognition via EEGNet in wireless sensing," in *Proc. 13th Int. Conf. Comput. Knowl. Eng.*, 2023, pp. 259–264.

[36] F. Nasser, A. Suliman, K. Poon, A. Alteneiji, and U. Ahmad, "Fall detection using Wi-Fi channel state information," in *Proc. 7th Int. Conf. Signal Process. Inf. Secur.*, 2024, pp. 1–5.

[37] Y. Li et al., "DiverSense: Maximizing Wi-Fi sensing range leveraging signal diversity," *Proc. ACM Interact. Mob. Wearable Ubiquitous Technol.*, vol. 6, no. 2, pp. 1–28, 2022.

[38] A. Pallaprolu, B. Korany, and Y. Mostofi, "Wiffract: A new foundation for RF imaging via edge tracing," in *Proc. 28th Annu. Int. Conf. Mobile Comput. And Netw.*, 2022, pp. 255–267.

[39] W. Shao and Y. Li, "An efficient method for modelling millimeter-wave scan for security screening of humans," *IEEE Trans. Comput. Imag.*, vol. 10, pp. 1616–1625, 2024.

[40] Y. Feng et al., "Analysis of polarization characteristics in outdoor-to-indoor wireless channels for high-speed trains," *IEEE Commun. Lett.*, vol. 29, no. 5, pp. 948–952, May 2025.

[41] W. Wang, A. X. Liu, M. Shahzad, K. Ling, and S. Lu, "Understanding and modeling of WiFi signal based human activity recognition," in *Proc. 21st Annu. Int. Conf. mobile Comput. Netw.*, 2015, pp. 65–76.

[42] Y. Xu, W. Yang, J. Wang, X. Zhou, H. Li, and L. Huang, "WiStep: Device-free step counting with WiFi signals," *Proc. ACM Interact. Mob. Wearable Ubiquitous Technol.*, vol. 1, no. 4, pp. 1–23, 2018.

[43] W. Chen and J. Chen, "Diffraction and scattering aware radio map and environment reconstruction using geometry model-assisted deep learning," *IEEE Trans. Wireless Commun.*, vol. 34, no. 12, pp. 19804–19819, Dec. 2024.

[44] M. G. Moghaddam, A. A. N. Shirehjini, and S. Shirmohammadi, "A WiFi-based method for recognizing fine-grained multiple-subject human activities," *IEEE Trans. Instrum. Meas.*, vol. 72, 2023, Art. no. 2520313.

Linqing Gui received the PhD degree in information science from INSA-Toulouse, Toulouse, France, in 2013. He is currently a professor and also PhD degree supervisor with the School of Computers, Nanjing University of Posts and Telecommunications, Nanjing, China. His research papers have been published in premium international journals and conferences, including IEEE Transactions on Mobile Computing, IEEE Transactions on Dependable and Secure Computing, IEEE Transactions on Vehicular Technology, ACM UbiComp and ACM MobiHoc. His research interests mainly include wireless sensing and mobile computing.

Yuting Yang received the BS degree from the College of Information Engineering, Dalian Ocean University, Dalian, China, in 2022. She is currently working toward the ME degree with the School of Computers, Nanjing University of Posts and Telecommunications, Nanjing, China. Her research interests include wireless sensing and mobile computing.

Yiping Zuo received the BS degree in electronic information science and technology from Huaiyin Normal University, Huaian, China, in 2015, the MS degree in communication and information systems from the Nanjing University of Posts and Telecommunications, Nanjing, China, in 2018, and the PhD degree in information and communications engineering from Southeast University, Nanjing, China, in 2022. She is currently with the Faculty of the School of Computer Science, Nanjing University of Posts and Telecommunications. Her research interests include ISAC, wireless sensing, and AIoT.

Fu Xiao received the PhD degree in computer science and technology from the Nanjing University of Science and Technology, Nanjing, China, in 2007. He is currently a professor and also PhD degree supervisor with the School of Computer Science, Nanjing University of Posts and Telecommunications, Nanjing. His research papers have been published in many prestigious conferences and journals, such as IEEE INFOCOM, IEEE/ACM Transactions on Networking, IEEE Journal on Selected Areas in Communications, IEEE Transactions on Mobile Computing, ACM MobiCom, ACM UbiComp, ACM Sensys and ACM MobiHoc. His research interests include the Internet of Things and mobile computing. He is a member of the IEEE Computer Society and the Association for Computing Machinery.

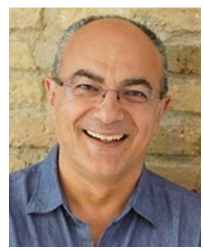

Schahram Dustdar (Fellow, IEEE) is currently a full professor of computer science (informatics) with a focus on internet technologies heading the Distributed Systems Group with TU Wien. He is founding co-editor-in-chief of *ACM Transactions on Internet of Things* and editor-in-chief of *Computing* (Springer). He is an associate editor for *IEEE Transactions on Services Computing*, *IEEE Transactions on Cloud Computing*, *ACM Computing Surveys*, *ACM Transactions on the Web*, and *ACM Transactions on Internet Technology*, and on the editorial board of *IEEE Internet Computing* and *IEEE Computer*. He was the recipient of multiple awards: TCI Distinguished Service Award in 2021, IEEE TCSVC Outstanding Leadership Award in 2018, IEEE TCSC Award for Excellence in Scalable Computing in 2019, ACM Distinguished Scientist in 2009, ACM Distinguished Speaker in 2021, and IBM Faculty Award in 2012.